

Deep End-to-end Adaptive k-Space Sampling, Reconstruction, and Registration for Dynamic MRI

George Yiasemis^{1,2}, Jan-Jakob Sonke^{1,2}, Jonas Teuwen^{1,2,3,*}

¹ Netherlands Cancer Institute, Amsterdam, Netherlands

² University of Amsterdam, Amsterdam, Netherlands

³ Radboud University Medical Center, Nijmegen, Netherlands

Abstract. Dynamic MRI enables a range of clinical applications, including cardiac function assessment, organ motion tracking, and radiotherapy guidance. However, fully sampling the dynamic k -space data is often infeasible due to time constraints and physiological motion such as respiratory and cardiac motion. This necessitates undersampling, which degrades the quality of reconstructed images. Poor image quality not only hinders visualization but also impairs the estimation of deformation fields, crucial for registering dynamic (moving) images to a static reference image. This registration enables tasks such as motion correction, treatment planning, and quantitative analysis, particularly in applications like cardiac imaging and MR-guided radiotherapy. To overcome the challenges posed by undersampling and motion, we introduce an end-to-end deep learning (DL) framework that integrates adaptive dynamic k -space sampling, reconstruction, and registration. Our approach begins with a DL-based adaptive sampling strategy, optimizing dynamic k -space acquisition to capture the most relevant data for each specific case. This is followed by a DL-based reconstruction module that produces images optimized for accurate deformation field estimation from the undersampled moving data. Finally, a registration module estimates the deformation fields aligning the reconstructed dynamic images with a static reference. The proposed framework is independent of specific reconstruction and registration modules allowing for plug-and-play integration of these components. The entire framework is jointly trained using a combination of supervised and unsupervised loss functions, enabling end-to-end optimization for improved performance across all components. Through controlled experiments and ablation studies, we validate each component, demonstrating that each choice contributes to robust motion estimation from undersampled dynamic data.

1 Introduction

Magnetic Resonance Imaging (MRI) is an essential imaging modality due to its non-invasive nature, absence of ionizing radiation, and exceptional soft tissue

* Corresponding author. Email: j.teuwen@nki.nl

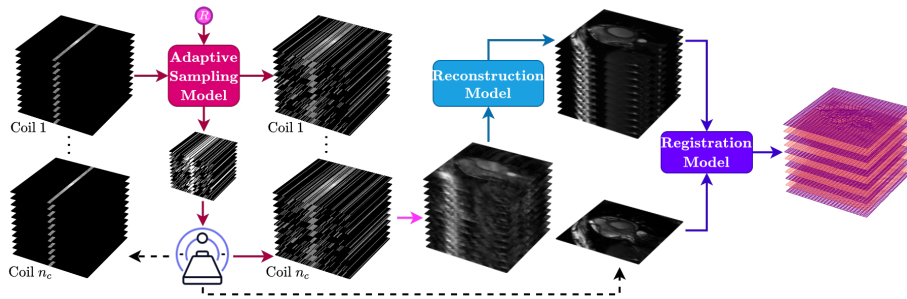


Fig. 1: Overview of our proposed pipeline: Utilizing initial dynamic (moving) k -space data, an adaptive sampling model generates a pattern tailored to a specific acceleration factor. This pattern is used to obtain undersampled moving k -space measurements, which are then fed into a reconstruction model to recover a high-fidelity moving image. Finally, the reconstructed dynamic image and a reference image are input into a registration model to predict motion patterns as registration fields.

contrast. Dynamic MRI serves a wide range of applications, including real-time tasks such as cardiac function assessment, motion tracking of various organs, and adaptive treatments in radiotherapy, making it indispensable in both diagnostic and treatment guidance. However, a major limitation of dynamic MRI is its inherently slow acquisition process, which becomes particularly challenging in real-time scenarios and is further exacerbated by voluntary or involuntary physiological motions such as respiration [8] and heartbeat [20].

Such motion can interfere with the ability to fully sample the k -space—the frequency domain data needed to reconstruct high-fidelity images in dynamic scenarios. To achieve artifact-free image reconstruction, the Nyquist sampling criterion (NC) [37] must be met, which specifies the minimum amount of data required to avoid aliasing and loss of fine detail. Although fully sampling the k -space per NC ensures spatial accuracy, it is often impossible. Thus, accelerating MRI acquisition by undersampling the k -space (below NC) becomes the only feasible approach. Even if dynamic acquisition is attainable in some cases, such as ECG-triggered cardiac MRI acquisition [30], undersampling can decrease operational costs and allow for more MRI scans.

Advancements in deep learning (DL) have markedly enhanced the reconstruction of undersampled MRI [33,11,32], demonstrating significant advantages over traditional methods like compressed sensing (CS) [29,15]. These methods leverage data-driven, often convolution-based, models to reconstruct high-quality images from limited k -space data, achieving superior reconstructions at high accelerations, and more efficient computations than CS.

Beyond reconstruction, DL methods have emerged for adaptively (under)sampling the MRI acquisition showing improved performance over non-adaptive learned, fixed or random sampling schemes. Although most methods have been explored

in the static case, only one DL approach has been devised specifically for dynamic MRI [61].

Nonetheless, undersampling the k -space inherently compromises image quality, which complicates the preservation of fine spatial details and may limit the accuracy of subsequent motion estimation and registration processes—essential for dynamic MRI applications. In cardiac MRI, for example, registration aligns images across phases to support motion correction, segmentation, etc, for comprehensive functional and structural assessment. [22]. In adaptive radiotherapy, MRI-based registration allows precise tumor motion tracking, thereby enabling accurate dose delivery while minimizing exposure to adjacent healthy tissues [19].

Several traditional and DL-based methods exist for image registration in medical imaging, with the goal of aligning a moving image to a reference frame and estimating motion [24,5,10,9,40]. Within the scope of accelerated MRI, some approaches have combined registration with a reconstruction step by co-optimizing both processes [13,41,42], while others employ learned motion models [53].

Motivated by the need for precise motion estimation in undersampled dynamic MRI, we introduce the first end-to-end DL-based framework that integrates adaptive undersampling, reconstruction, and registration for dynamic MRI. An overview of our method is depicted in Fig. 1. Our contributions are as follows:

- We introduce a novel end-to-end pipeline that integrates adaptive undersampling, reconstruction, and registration for dynamic MRI—a comprehensive approach that, to our knowledge, has not been explored in any similar DL-based or traditional optimization framework.
- We present a detailed methodology covering all components of our approach, ensuring reproducibility for each module. Code will be made available.
- We rigorously evaluate our framework under various configurations.
- We validate our approach on a cardiac cine dataset and demonstrate its generalizability on out-of-distribution data (aorta dataset).

The rest of the paper is organized as follows: Section 2 covers background and related work, Section 3 details our methodology, Section 4 presents our experimental setup and results, and Section 5 offers a discussion and conclusions.

2 Background and Related work

2.1 Dynamic MRI Reconstruction

Dynamic MRI reconstruction aims to recover a moving image $\mathbf{x} \in \mathbb{C}^{n \times n_t}$ from acquired dynamic k -space data, where $n = n_x \times n_y$ denotes the spatial dimensions, n_c represents the number of scanner coils, and n_t the temporal dimension of the sequence. Given fully sampled data $\mathbf{y} \in \mathbb{C}^{n \times n_c \times n_t}$, the underlying image sequence can be obtained by applying the inverse Fast Fourier Transform \mathcal{F}^{-1} ,

followed by the root-sum-of-squares (RSS) as follows:

$$\mathbf{x}_{\cdot,\tau} := \text{RSS} \circ \mathcal{F}^{-1}(\mathbf{y}_{\cdot,\tau}), \quad \tau = 1, \dots, n_t, \quad (1)$$

where,

$$\text{RSS}(\mathbf{w}) = \left(\sum_{k=1}^{n_c} |\mathbf{w}_{\cdot,k}|^2 \right)^{1/2} \in \mathbb{R}^n, \quad \mathbf{w} \in \mathbb{C}^{n \times n_c}. \quad (2)$$

Here, $|\mathbf{a}| := \sqrt{\text{real}(\mathbf{a})^2 + \text{imag}(\mathbf{a})^2}$, denotes the modulus operator. To reduce the MRI acquisition time, undersampling is applied to the k -space: $\tilde{\mathbf{y}}^{\mathbf{M}} := \mathbf{M}(\mathbf{y})$. Undersampling is characterized by a binary mask operator $\mathbf{M} = (\mathbf{M}_1, \dots, \mathbf{M}_{n_t}) \in \{0, 1\}^{n \times n_t}$, which zeros-out non-acquired k -space samples as follows:

$$\tilde{\mathbf{y}}_{i,k,\tau}^{\mathbf{M}} = (\mathbf{M}(\mathbf{y}))_{i,k,\tau} := \begin{cases} \mathbf{y}_{i,k,\tau} & \text{if } (\mathbf{M}_\tau)_i = 1 \\ 0, & \text{if } (\mathbf{M}_\tau)_i = 0, \end{cases} \quad (3)$$

$$i = 1, \dots, n, \quad k = 1, \dots, n_c, \quad \tau = 1, \dots, n_t.$$

The resulting forward model for each frame τ of the sequence is described by the forward operator $\mathcal{T}_{\mathbf{M}_\tau, \mathbf{S}_\tau}$:

$$\tilde{\mathbf{y}}_{\cdot,\tau}^{\mathbf{M}} = \mathcal{T}_{\mathbf{M}_\tau, \mathbf{S}_\tau}(\mathbf{x}_\tau) := \mathbf{M}_\tau \circ \mathcal{F} \circ \mathcal{C}_{\mathbf{S}_\tau}(\mathbf{x}_{\cdot,\tau}), \quad (4)$$

where $\mathcal{C}_{\mathbf{S}_\tau}$ denotes the coil sensitivity-encoding operator, which decomposes an image into individual coil images using coil sensitivity profiles $\mathbf{S}_\tau \in \mathbb{C}^{n^2 \times n_c}$ that represent the spatial sensitivity of each coil. This is expressed as:

$$\mathcal{C}_{\mathbf{S}_\tau}(\mathbf{z}) = (\mathbf{S}_\tau^1 \mathbf{z}, \dots, \mathbf{S}_\tau^{n_c} \mathbf{z}), \quad \text{for } \mathbf{z} \in \mathbb{C}^n. \quad (5)$$

A reconstruction for (4) can be formulated as a solution to a regularized least squares optimization problem:

$$\underset{\mathbf{x}' \in \mathbb{C}^{n \times n_t}}{\text{argmin}} \sum_{\tau=1}^{n_t} \frac{1}{2} \|\mathcal{T}_{\mathbf{M}_\tau, \mathbf{S}_\tau}(\mathbf{x}'_{\cdot,\tau}) - \tilde{\mathbf{y}}_{\cdot,\tau}^{\mathbf{M}}\|_2^2 + \mathcal{H}(\mathbf{x}'), \quad (6)$$

where \mathcal{H} denotes an arbitrary regularization functional, which introduces prior domain knowledge.

2.2 Deep Learning-based MRI Reconstruction

Deep learning methods have been widely applied to address accelerated MRI, bypassing the need for handcrafted priors and computationally intensive optimization techniques in CS. DL methods primarily fall into two categories: direct mapping and unrolled optimization approaches [11]. Direct mapping DL methods take undersampled images as input and learn to output reconstructed images, a straightforward approach that typically requires a substantial amount of training data. In contrast, unrolled optimization methods are inspired by

compressed sensing techniques and leverage algorithms like gradient descent [17,39,60], primal-dual descent [1], conjugate gradient [2], and ADMM [58] to iteratively solve (6).

The availability of open-access k -space datasets from challenges such as fastMRI [23], Multi-Coil MRI Reconstruction [6], and the recent CMRxRecon 2023 and 2024 [49,50], has empowered the community to pursue data-driven approaches. Consequently, numerous DL-based reconstruction techniques have been developed, primarily for static MRI acquisitions [14,39,60], with a recent growing expansion into dynamic settings [63,46,56,27].

2.3 Adaptive MRI Acquisition

Several methods have been proposed to replace standard sampling patterns (e.g., equidistant, random uniform, Gaussian [59]) in DL-based MRI reconstruction with learned approaches. These methods include training dataset-based sampling optimization [3,65,38] and adaptive, case-specific patterns [4,16] jointly learned with reconstruction networks. While most focus on static MRI, [61] extends adaptive sampling to dynamic (2D + time) imaging through an end-to-end approach for adaptive dynamic undersampling and reconstruction (E2E-ADS-Recon).

Unlike previous methods optimized for single acceleration factors, this approach is proposed to be flexible across various acceleration factors. It includes two possible configurations for adapted undersampling: a phase-specific approach, where distinct patterns are generated for each temporal phase, and a unified approach, applying a single pattern across all phases.

2.4 Deformable Image Registration

Deformable (non-rigid) registration aims to align a moving image $\mathbf{z}_{\text{mov}} \in \mathbb{R}^{n \times n_t}$, to a fixed, static reference image $\mathbf{z}_{\text{ref}} \in \mathbb{R}^n$, by estimating spatial deformation fields $\phi = (\phi_1, \dots, \phi_{n_t}) \in \mathbb{R}^{2 \times n \times n_t}$.

The displacement field ϕ_τ maps the coordinates of \mathbf{z}_{ref} to those of $(\mathbf{z}_{\text{mov}})_\tau$, achieved through a warping operation, $\mathcal{W} : \mathbb{R}^n \times \mathbb{R}^{2 \times n} \rightarrow \mathbb{R}^n$ [5], enabling the registration of \mathbf{z}_{mov} :

$$\mathbf{z}_{\text{reg}} = \left\{ \mathcal{W}((\mathbf{z}_{\text{mov}})_{\cdot,\tau}, \phi_\tau) \right\}_{\tau=1}^{n_t} \in \mathbb{R}^{n \times n_t}. \quad (7)$$

The objective is to determine an optimal deformation field, ϕ^* , that aligns the moving image with the reference accurately. This is often posed as an unsupervised minimization problem using a similarity measure \mathcal{L}_{sim} :

$$\phi^* := \arg \min_{\phi} \mathcal{L}_{\text{sim}}(\mathbf{z}_{\text{reg}}, \mathbf{z}_{\text{ref}}). \quad (8)$$

Several approaches also leverage complementary (supervised) tasks to enhance the registration process, incorporating segmentation accuracy losses when ground truth delineations of target organs are available [18,5].

In this work we only employ a similarity measure as in (7) due to the absence of such segmentations within our datasets.

3 Methods

3.1 Deep Learning Framework

Sensitivity Profiles Estimation Following [39], we begin by estimating sensitivity profiles for the multi-coil data, denoted as $\tilde{\mathbf{S}} \in \mathbb{C}^{n^2 \times n_c \times n_t}$, using a fully-sampled central region of the k -space, $\tilde{\mathbf{y}}_{\text{mov}}^{\text{M}^{\text{acs}}}$ corresponding to low frequencies—the autocalibration signal (ACS). Consistent with [39], these estimates are then input into a DL-based model, specifically a two-dimensional U-Net [35], denoted as \mathcal{S}_σ , which is trained to refine them:

$$\mathbf{S}_\tau^k := \mathcal{S}_\sigma(\tilde{\mathbf{S}}_\tau^k), \quad \tau = 1, \dots, n_t, \quad k = 1, \dots, n_c. \quad (9)$$

The refined sensitivity profiles are subsequently normalized to satisfy:

$$\sum_{k=1}^{n_c} (\mathbf{S}_\tau^k)^* \mathbf{S}_\tau^k = \mathbf{I}_n \in \mathbb{R}^{n \times n}. \quad (10)$$

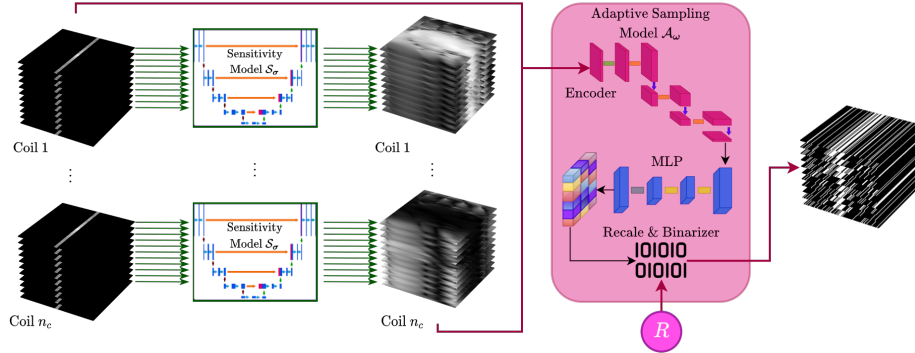


Fig. 2: Adaptive Sampling Model (\mathcal{A}_ω) framework. Sensitivity profiles from the sensitivity model (\mathcal{S}_σ) and initial undersampled moving data ($\tilde{\mathbf{y}}_{\text{mov}}^{\text{M}^0}$) are processed by a U-Net-like encoder followed by a MLP, generating sampling probabilities. These are rescaled for the specified acceleration R and binarized via a straight-through estimator creating an adapted binary dynamic sampling mask. Here we assume $\tilde{\mathbf{y}}_{\text{mov}}^{\text{M}^0} = \tilde{\mathbf{y}}_{\text{mov}}^{\text{M}^{\text{acs}}}$.

Adaptive Sampling Model An adaptive dynamic sampling (ADS) module, inspired by the E2E-ADS-Recon framework [61], denoted as \mathcal{A}_ω , takes as input initially undersampled moving data $\tilde{\mathbf{y}}_{\text{mov}}^{\text{M}^0}$, acquired with an initial mask \mathbf{M}^0 , along with sensitivity profiles \mathbf{S} and a target acceleration factor R . ADS consists of cascades of 3D U-Net-like encoders and multi-layer perceptrons (MLPs) to

generate sampling selection probabilities, which are binarized using a straight-through estimator [7,62] to match the sampling budget and enable adaptive sampling according to the target acceleration R .

This module outputs a binary mask operator $\mathbf{M} = (\mathbf{M}_1, \dots, \mathbf{M}_{n_t})$, which guides the subsequent dynamic image reconstruction:

$$\mathbf{M} := \mathcal{A}_\omega(\tilde{\mathbf{y}}_{\text{mov}}^{\mathbf{M}^0}; \mathbf{S}, R). \quad (11)$$

By default, the ACS data $\tilde{\mathbf{y}}_{\text{mov}}^{\mathbf{M}^0} = \tilde{\mathbf{y}}_{\text{mov}}^{\mathbf{M}^{\text{acs}}}$ initializes \mathcal{A}_ω , unless otherwise specified.

Reconstruction Model Our proposed pipeline (see Sec. 3.2) is agnostic to the choice of reconstruction network, supporting any DL-based dynamic reconstruction model. For the main experiments, we use the variable Splitting Half-quadratic ADMM algorithm for Reconstruction of inverse-Problems (vSHARP) [58], a model that demonstrated competitive performance in both reconstruction quality and speed at the CMRxRecon challenge 2023 [49]. The vSHARP model unrolls a DL-based optimization over T iterations. Denoted as \mathcal{V}_θ , it accepts an undersampled dynamic image $\tilde{\mathbf{x}}_{\text{mov}}^{\mathbf{M}}$ and sensitivity maps \mathbf{S} to yield a refined dynamic reconstruction:

$$\hat{\mathbf{x}}_{\text{mov}} = \mathcal{V}_\theta(\tilde{\mathbf{x}}_{\text{mov}}^{\mathbf{M}}; \mathbf{S}), (\hat{\mathbf{x}}_{\text{mov}}^{\mathbf{M}})_{\cdot, \tau} = \mathcal{R}_{\mathbf{S}_\tau} \circ \mathcal{F}^{-1}(\tilde{\mathbf{y}}_{\text{mov}}^{\mathbf{M}})_{\cdot, \tau}. \quad (12)$$

The operator $\mathcal{R}_{\mathbf{S}_\tau} : \mathbb{C}^{n \times n_c} \rightarrow \mathbb{C}^n$ represents the coil-combining operator using \mathbf{S}_τ :

$$\mathcal{R}_{\mathbf{S}_\tau}(\mathbf{v}) := \sum_{k=1}^{n_c} (\mathbf{S}_\tau^k)^* \mathbf{v}_{\cdot, k} \in \mathbb{C}^n, \quad \text{for } \mathbf{v} \in \mathbb{C}^{n \times n_c}. \quad (13)$$

Additional details on the reconstruction network are provided in Appendix A.

Registration - Motion Estimation Model As with Sec. 3.1, any deformable image registration method—DL-based or otherwise—can be employed to estimate deformation fields for each temporal phase of the moving image relative to a reference image. For the main experiments, we use a lightweight approach by using a two-dimensional U-Net [35], denoted as \mathcal{R}_ψ , which processes a concatenated along the channel dimension input of the (reconstructed) moving image and the reference image $\mathbf{x}_{\text{ref}} \in \mathbb{R}^n$, rather than using, for instance, a 3D U-Net. This setup configures the initial layer to accept $n_t + 1$ input channels, with the model outputting $2 \times n_t$ channels, representing the deformation fields for each temporal phase of the moving image relative to the reference image:

$$\phi = \mathcal{R}_\psi(\mathbf{w}), \quad \mathbf{w} = [|\hat{\mathbf{x}}_{\text{mov}}|, \mathbf{x}_{\text{ref}}] \in \mathbb{R}^{n \times (n_t + 1)}. \quad (14)$$

3.2 End-to-End Framework

Our end-to-end framework incorporates sensitivity estimation, adaptive sampling, reconstruction, and registration in a sequential pipeline, as outlined in the

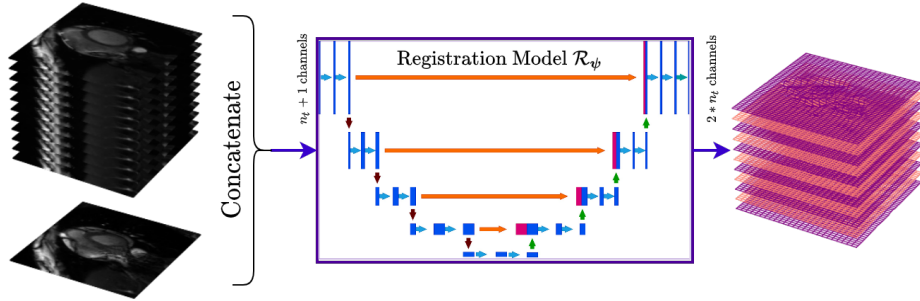


Fig. 3: A 2D U-Net plays the role of the registration model. It takes as input the reconstructed moving and reference images, concatenated along the channel dimension. The registration model outputs a sequence of registration fields corresponding to the displacements/motion between the moving and reference images.

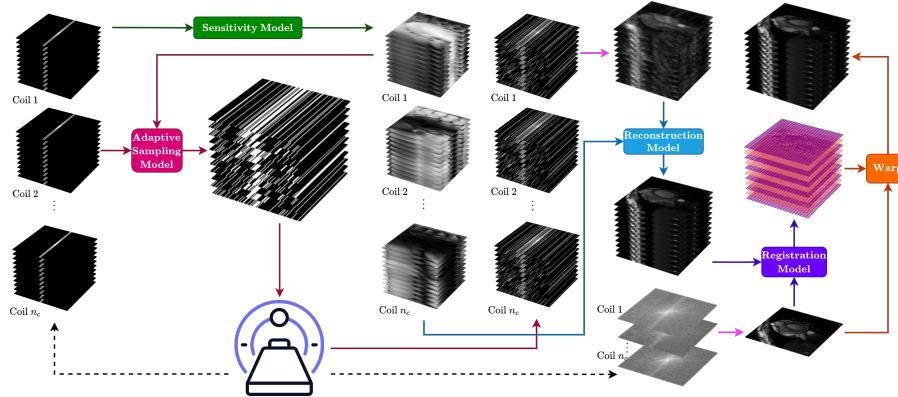


Fig. 4: End-to-end pipeline of the proposed method. The process starts with coil sensitivity profile estimation from ACS data. Next, the adaptive sampling model selects optimized sampling patterns based on initial moving data (here equivalent to ACS data) and sensitivities. The adaptively acquired data are then input into the reconstruction model. Finally, the registration model outputs deformation fields that align the reconstructed sequence to a reference accounting for motion. A registered output (through warping) is used for loss computation.

previous sections. First, sensitivity profiles \mathbf{S} are estimated and refined using \mathcal{S}_σ . These refined sensitivity maps \mathbf{S} , together with the initial undersampled k -space data $\tilde{\mathbf{y}}_{\text{mov}}^{\mathbf{M}^0}$, inform the adaptive sampling model \mathcal{A}_ω , which generates dynamic sampling patterns \mathbf{M} based on the specified acceleration factor R . The adaptively sampled moving data $\tilde{\mathbf{y}}_{\text{mov}}^{\mathbf{M}}$ is then processed by the reconstruction model \mathcal{V}_θ , to obtain a high-quality dynamic image. Finally, the registration model \mathcal{R}_ψ calculates deformation fields to align the reconstructions with a reference frame,

correcting for motion and ensuring temporal consistency across frames. The full pipeline is presented in Algorithm 1 and illustrated in Figure 4.

Algorithm 1: End-to-end Adaptive Sampling, Reconstruction and Registration for Dynamic MRI

Input: $\tilde{\mathbf{y}}_{\text{mov}}^{\text{M}^0}, \tilde{\mathbf{y}}_{\text{mov}}^{\text{M}^{\text{acs}}} \in \mathbb{C}^{n \times n_c \times n_t}$, R , $\mathbf{y}_{\text{ref}} \in \mathbb{C}^{n \times n_c}$
Output: $\phi \in \mathbb{R}^{2 \times n \times n_t}$, [Optional] $\mathbf{x}_{\text{reg}} \in \mathbb{R}^{n \times n_t}$

- 1 **for** $\tau \leftarrow 1$ **to** n_t **do**
- 2 **for** $k \leftarrow 1$ **to** n_c **do**
- 3 Estimate $\tilde{\mathbf{S}}_\tau^k$ from $(\tilde{\mathbf{y}}_{\text{mov}}^{\text{M}^{\text{acs}}})_{\cdot, k, \tau}$ as in [39]
- 4 $\mathbf{S}_\tau^k \leftarrow \mathcal{S}_\sigma(\tilde{\mathbf{S}}_\tau^k)$ // Refine Sensitivities
- 5 Normalize s.t. $\sum_{k=1}^{n_c} (\mathbf{S}_\tau^k)^* \mathbf{S}_\tau^k \leftarrow \mathbf{I}_n \in \mathbb{R}^{n \times n}$
- 6 **end**
- 7 **end**
- 8 $\mathbf{M} \leftarrow \mathcal{A}_\omega(\tilde{\mathbf{y}}_{\text{mov}}^{\text{M}^0}; \mathbf{S}, R)$ // Adapt sampling pattern
- 9 $\tilde{\mathbf{y}}_{\text{mov}}^{\text{M}} \leftarrow \mathbf{M}(\mathbf{y}_{\text{mov}})$ // Sample moving data with M
- 10 **for** $\tau \leftarrow 1$ **to** n_t **do**
- 11 $(\tilde{\mathbf{x}}_{\text{mov}}^{\text{M}})_{\cdot, \tau} \leftarrow \mathcal{R}_{\mathbf{S}_\tau} \circ \mathcal{F}^{-1}(\tilde{\mathbf{y}}_{\text{mov}}^{\text{M}})_{\cdot, \tau}$
- 12 **end**
- 13 $\hat{\mathbf{x}}_{\text{mov}} \leftarrow \mathcal{V}_\theta(\tilde{\mathbf{x}}_{\text{mov}}^{\text{M}}; \mathbf{S})$ // Reconstruct moving image
- 14 $\mathbf{x}_{\text{ref}} \leftarrow \text{RSS} \circ \mathcal{F}^{-1}(\mathbf{y}_{\text{ref}})$
- 15 $\mathbf{w} \leftarrow [|\hat{\mathbf{x}}_{\text{mov}}|, \mathbf{x}_{\text{ref}}]$ // Concatenate along channel dim
- 16 $\phi \leftarrow \mathcal{R}_\psi(\mathbf{w})$ // Compute registration field
- 17 [Optional] **for** $\tau \leftarrow 1$ **to** n_t **do**
- 18 $(\mathbf{x}_{\text{reg}})_{\cdot, \tau} \leftarrow \mathcal{W}(|\hat{\mathbf{x}}_{\text{mov}}|_{\cdot, \tau}, \phi_\tau)$ // Warp mov. image
- 19 **end**

3.3 Training Loss Function

With the end-to-end framework established, the primary objective is to optimize the registration task, specifically enhancing the accuracy of the deformation fields. Although the reconstruction task is secondary, we expect that improving the image reconstruction indirectly supports better motion estimation by providing high-fidelity inputs for alignment.

Let $\tilde{\mathbf{y}}_{\text{mov}}^{\text{M}} \in \mathbb{C}^{n \times n_c \times n_t}$ represent the undersampled moving data, acquired using the predicted sampling set \mathbf{M} from \mathcal{A}_ω . Also let $\mathbf{y}_{\text{mov}} \in \mathbb{C}^{n \times n_c \times n_t}$ and $\mathbf{y}_{\text{ref}} \in \mathbb{C}^{n \times n_c}$ denote the fully sampled (moving) and reference k -space measurements. The total loss we aim to optimize is given by:

$$\mathcal{L} := \alpha \mathcal{L}_{\text{rec}} + \beta \mathcal{L}_{\text{reg}}, \quad (15)$$

where $\alpha, \beta > 0$ weight the reconstruction and registration losses. The reconstruction loss is defined as:

$$\mathcal{L}_{\text{rec}} = \mathcal{L}_{\text{ssim}}(|\hat{\mathbf{x}}_{\text{mov}}|, \mathbf{x}_{\text{mov}}) + \left\| |\hat{\mathbf{x}}_{\text{mov}}| - \mathbf{x}_{\text{mov}} \right\|_1, \quad (16)$$

with $\hat{\mathbf{x}}_{\text{mov}} = \mathcal{V}_{\theta}(\tilde{\mathbf{y}}_{\text{mov}}^{\text{M}}; \mathbf{S})$ representing the predicted moving image and $\mathbf{x}_{\text{mov}} = \text{RSS} \circ \mathcal{F}(\mathbf{y}_{\text{mov}})$ denoting the ground truth. Here, $\mathcal{L}_{\text{ssim}} := \mathcal{L}_{\text{ssim}2\text{D}} + \mathcal{L}_{\text{ssim}3\text{D}}$ combines 2D and 3D structural similarity index measure (SSIM) losses [58], calculated over individual slices and across the sequence, respectively. For the registration loss \mathcal{L}_{reg} , we focus on aligning the registered reconstructed moving and reference images while ensuring a smooth deformation field. This includes a similarity term for image alignment and a regularization term to constrain the registration field:

$$\mathcal{L}_{\text{reg}} = \mathcal{L}_{\text{sim}}(\mathbf{x}_{\text{reg}}, \{\mathbf{x}_{\text{ref}}\}_{t=1}^{n_t}) + \mathcal{L}_{\text{smooth}}(\phi), \quad (17)$$

where $\mathbf{x}_{\text{reg}} = \{\mathcal{W}(|\hat{\mathbf{x}}_{\text{mov}}|_{\cdot, \tau}, \phi_{\tau})\}_{\tau=1}^{n_t} \in \mathbb{R}^{n \times n_t}$ and $\mathbf{x}_{\text{ref}} = \text{RSS} \circ \mathcal{F}(\mathbf{y}_{\text{ref}}) \in \mathbb{R}^n$. Note that $\{\mathbf{x}_{\text{ref}}\}_{t=1}^{n_t} \in \mathbb{R}^{n \times n_t}$ denotes \mathbf{x}_{ref} repeated n_t times. For \mathcal{L}_{sim} , we apply the same loss functions as in (16), and $\phi = \mathcal{R}_{\psi}(|\hat{\mathbf{x}}_{\text{mov}}|, \mathbf{x}_{\text{ref}})$ denotes the registration field prediction.

The smoothness term, inspired by a diffusion regularizer [12,5], $\mathcal{L}_{\text{smooth}}$, aims to regularize the registration field by penalizing abrupt changes, approximating partial derivatives along each dimension through mean absolute finite differences:

$$\mathcal{L}_{\text{smooth}}(\phi) = \frac{1}{2nn_t} \sum_{\tau} \sum_{\mathbf{p}} \left| \frac{\partial \phi_{\tau}(\mathbf{p})}{\partial u_1} \right| + \left| \frac{\partial \phi_{\tau}(\mathbf{p})}{\partial u_2} \right|, \quad (18)$$

where $\frac{\partial \phi_{\tau}(\mathbf{p})}{\partial u_i}$ denotes the approximated partial derivatives.

4 Experiments

4.1 Datasets

We used the CMRxRecon 2023 cardiac cine dataset [49,48], which comprises 472 scans with fully sampled, ECG-triggered multi-coil ($n_c = 10$) k -space data, totaling 3,185 2D sequences, with the cardiac cycle segmented into 12 temporal frames. For external validation, we used the aorta dataset from CMRxRecon 2024 [50], also ECG-triggered with $n_c = 10$ coils and 12-frame cycles. The inference subset comprises 111 scans and 1,332 sequences.

4.2 Undersampling

Undersampling was applied retrospectively in all experiments, with fully sampled data used for loss calculation and evaluation. A 4% center fraction within the ACS was retained. Training used arbitrary acceleration factors of $4\times$, $6\times$, or $8\times$, and all three were evaluated during inference.

4.3 Selection of Registration Reference

Each sequence contained 12 segments of the cardiac cycle. We selected the 6th segment as registration reference $\mathbf{y}_{\text{ref}} \in \mathbb{C}^{n \times n_c}$, corresponding to the end-systolic (contracted) phase, since this phase can be consistently triggered by ECG [31], providing a stable anatomical structure. The remaining segments ($n_t = 11$) served as the moving image target $\mathbf{y}_{\text{mov}} \in \mathbb{C}^{n \times n_c \times n_t}$, which were retrospectively undersampled to create the undersampled moving input, $\tilde{\mathbf{y}}_{\text{mov}}^{\mathbf{M}}$.

4.4 Evaluation

We assess estimated motion quality by evaluating the similarity of the registered moving images (warped reconstructed images using predicted deformation fields) to the reference image. We employ three image quality metrics: SSIM, PSNR, and NMSE. For brevity, definitions are provided in Appendix B. For each metric m , we averaged results across all phases of the sequence:

$$\bar{m} = \frac{1}{n_t} \sum_{\tau=1}^{n_t} m\left(\mathcal{W}(|\hat{\mathbf{x}}_{\text{mov}}|_{\cdot, \tau}, \phi_{\tau}), \mathbf{x}_{\text{ref}}\right). \quad (19)$$

4.5 Training and Optimization Details

Models were implemented in PyTorch [34] and trained on single NVIDIA A100 or H100 GPUs with the Adam optimizer (no weight decay) [66], a batch size of 1, and a learning rate schedule with a 10k step size and 0.8 decay. After a 2k-iteration linear warm-up to reach a 3e-3 learning rate, training continued for 52k iterations. The best checkpoint, based on validation SSIM, was used for inference.

4.6 Ablation and Component Analysis

Our proposed pipeline is the first to integrate adaptive sampling, reconstruction, and registration into an end-to-end framework for dynamic MRI, making direct comparisons with existing baselines impossible. Therefore, we evaluate each key component within our approach through ‘‘controlled’’ comparisons and ablation studies.

Baseline Setup Our baseline setup includes:

- Sensitivity Model: four scales (16, 32, 64, 128 filters).
- Adaptive Sampling Module: Identical to [61] in hyperparameters, but with one cascade instead of two. Unless specified otherwise, adaptive sampling is phase-specific. We employ ACS data for initialization ($\tilde{\mathbf{y}}_{\text{mov}}^{\mathbf{M}^0} = \tilde{\mathbf{y}}_{\text{mov}}^{\mathbf{M}^{\text{ACS}}}$).
- Reconstruction Model: vSHARP with $T = 10$ optimization steps utilizing 3D U-Nets with four scales (16, 32, 64, and 128 filters) and $T_x = 6$ data consistency steps. Other parameters match [58].
- Registration Model: A 2D U-Net (see Section 3.1) with four scales (16, 32, 64, and 128 filters).

- End-to-end training loss calculation with $\alpha = \beta = 1$, reflecting the expectation that improving reconstruction quality will contribute to reliable registration by reducing artifacts and inconsistencies that could otherwise impair motion estimation.

In each experiment, only the evaluated component is modified, keeping all other settings constant to isolate its effect.

Registration Component To assess our lightweight registration approach (concatenating moving and reference images along the channel dimension in a 2D U-Net), we compare it against DL-based alternatives:

- 1) A standard registration method - VoxelMorph [5]
- 2) A vision transformer-based registration method following TransMorph [9]
- 3) Our proposed model using a larger U-Net and traditional motion estimation methods:
- 4) Optical flow with iterative Lucas-Kanade (ILK) [25] and TV- L_1 [64] solvers from `scikit-image` [47]
- 5) DEMONS registration algorithm [43] provided by SimpleITK [28]

See Appendix B for the choice of hyperparameters.

Reconstruction Component To evaluate the choice of reconstruction network (vSHARP) and showcase the pipeline’s modularity, we also test a state-of-the-art model, the End-to-End Variational Network (VarNet) [39] (extended to 3D), configured with 10 cascades and 3D U-Nets as regularizers (4 scales: 32, 64, 128, 256 filters).

Adaptive Sampling Component

- **Initialization** The ADS module relies on initial data $\tilde{\mathbf{y}}_{\text{mov}}^{\mathbf{M}^0}$ to guide the acquisition. In [61], equispaced initialization improved reconstruction quality; we evaluate this for registration quality as well (initial data, include ACS and accelerated at $(R - 4) \times$ where R is the target acceleration).
- **Phase-specific vs Unified Sampling** Phase-specific experiments generate a unique adaptive pattern for each temporal phase, whereas unified settings produce a single pattern for all phases.
- **Learned vs Fixed Sampling** We compare our pipeline by replacing the adaptive sampling module with non-adaptive dataset-optimized [65], fixed non-adaptive equispaced [59] (distinct pattern per frame in phase-specific experiments; same for all frames in unified settings) and kt -equispaced [44] (temporally interleaved trajectory, applicable only to phase-specific) sampling schemes. Offset of patterns was randomly selected during training and fixed (per case) during inference.

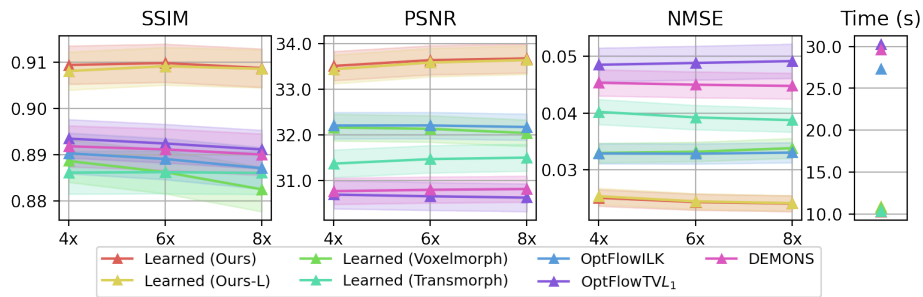
Weighting Parameters for Joint Loss To investigate how task weighting impacts registration quality, we set the weighting parameters in (15) to $\alpha = 1$, $\beta = 3$. This allows us to examine the extent to which additional emphasis on the registration task influences the final motion estimation.

Joint vs. Decoupled Training To evaluate task interactions, we adopt a decoupled loss approach. For the registration loss \mathcal{L}_{reg} , only the registration model parameters (ψ) are updated, while holding all others constant (frozen). Conversely, for the reconstruction loss \mathcal{L}_{rec} , only the parameters σ , ω , and θ of the sensitivity, sampling, and reconstruction models are optimized, while ψ remains fixed. This decoupling allows each task to be evaluated independently, compared to our original joint, end-to-end training.

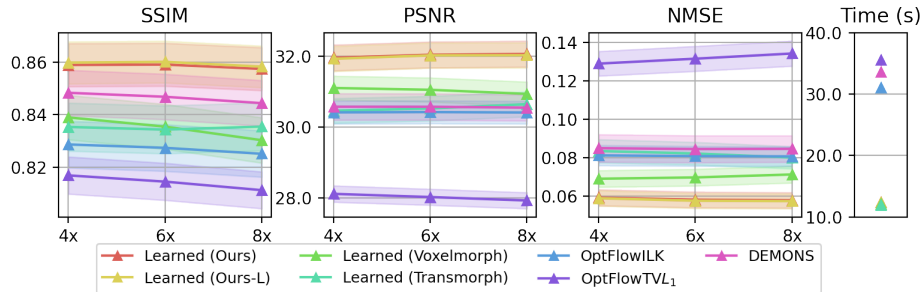
4.7 Experimental Results

We present average quantitative results for each experiment across both datasets (cine - seen during training, aorta - unseen), displayed as line graphs (function of acceleration factor) with ± 0.1 standard deviations, along with average inference times.

Detailed results are also in tabular form in Appendix C. Examples of qualitative results are provided in Figure 10, with further examples in Appendix C.



(a) Cine test dataset.



(b) Aorta dataset (not seen during training).

Fig. 5: Comparison of registration performance across different methods.

Registration Component Figure 5 presents the registration performance of our pipeline across various registration modules, evaluated on both datasets. Across

all acceleration factors ($4\times$, $6\times$, $8\times$), our proposed lightweight model consistently outperforms traditional methods (OptFlow ILK, TV- L_1 , DEMONS) and the two considered DL-based approaches (Voxelmorph, Transmorph) in all metrics on both datasets, indicating more accurate motion estimation. Notably, the larger variant of our lightweight model did not improve registration. Additionally, our pipeline with learned registration methods (including ours) achieves significantly lower inference times than non-DL-based methods.

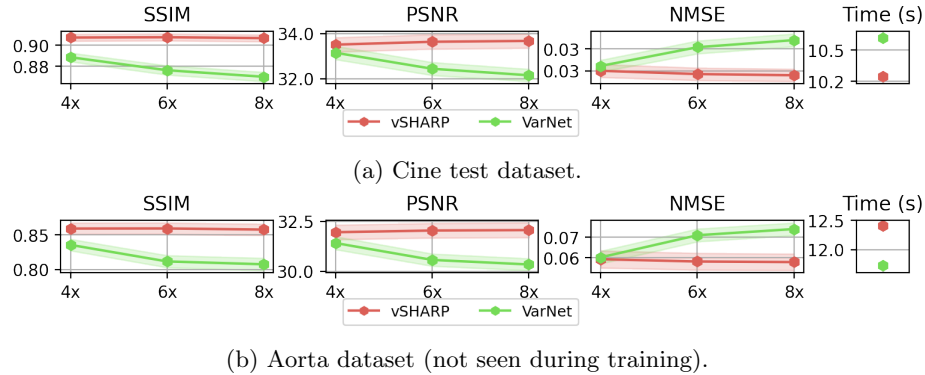
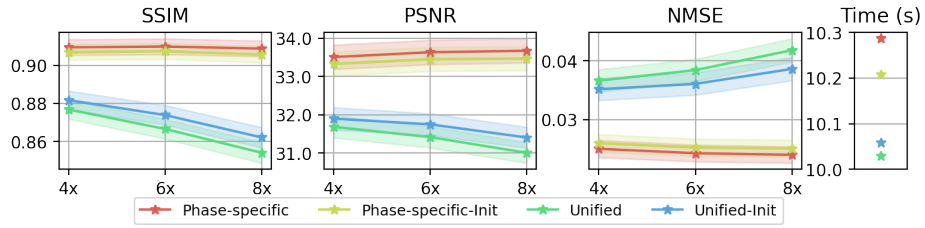


Fig. 6: Impact of reconstruction model on registration results.

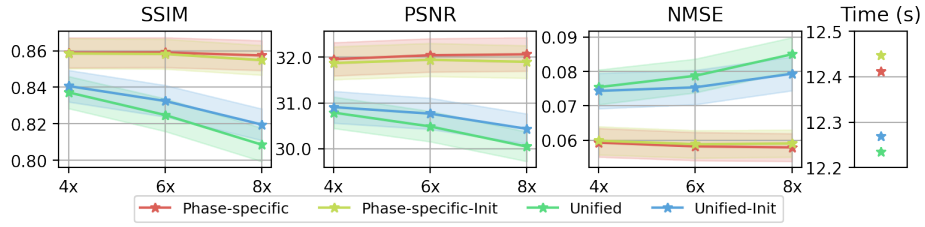
Reconstruction Component Figure 6 shows that replacing vSHARP with VarNet yields lower registration metrics, suggesting vSHARP’s optimization-based design better supports accurate motion estimation in our pipeline.

Adaptive Sampling Component In Figure 7 we compare the effects of phase-specific versus unified adaptive sampling with both ACS initialization and equispaced-fused ACS initialization. Phase-specific sampling consistently outperforms unified sampling across all metrics, particularly at higher accelerations, indicating better registration quality with unique trajectories per phase. In contrast to the reconstruction quality findings in [61], equispaced initialization did not notably benefit registration quality. Figure 8 further shows that learned sampling (adaptive, dataset-optimized) outperforms fixed schemes across all metrics with minimal inference time impact, with dataset-optimized sampling showing a slight advantage over adaptive.

Weighting Parameters for Joint Loss Although the reconstruction quality of the moving image is not a primary focus, we examine the effect of varying loss weights on both reconstruction and registration tasks in Figure 9. Results show that a higher registration weight ($\beta = 3$) noticeably reduces reconstruction quality, yet registration accuracy improves across all metrics and undersampling rates.

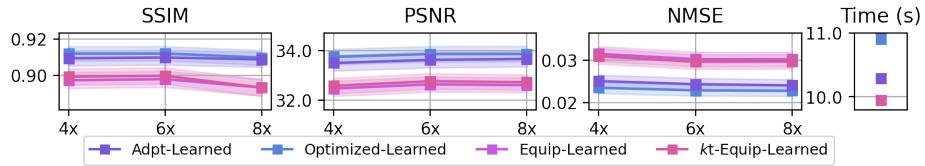


(a) Cine test dataset.

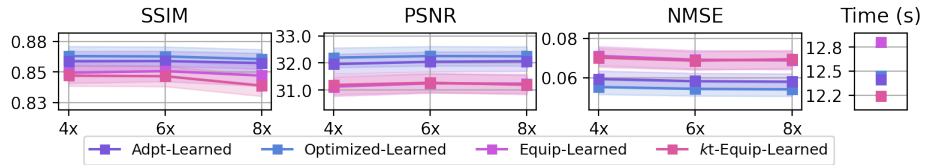


(b) Aorta dataset (not seen during training).

Fig. 7: Impact of phase-specific vs unified adaptive sampling with ACS and equispaced initialization on registration results.



(a) Cine test dataset.



(b) Aorta dataset (not seen during training).

Fig. 8: Impact of learned vs fixed non-adaptive sampling schemes on registration results.

Joint vs. Decoupled Training The results in Figure 9 further reveal that the joint training approach performs slightly better in terms of both, reconstruction and registration, than the decoupled method for equal weighting.

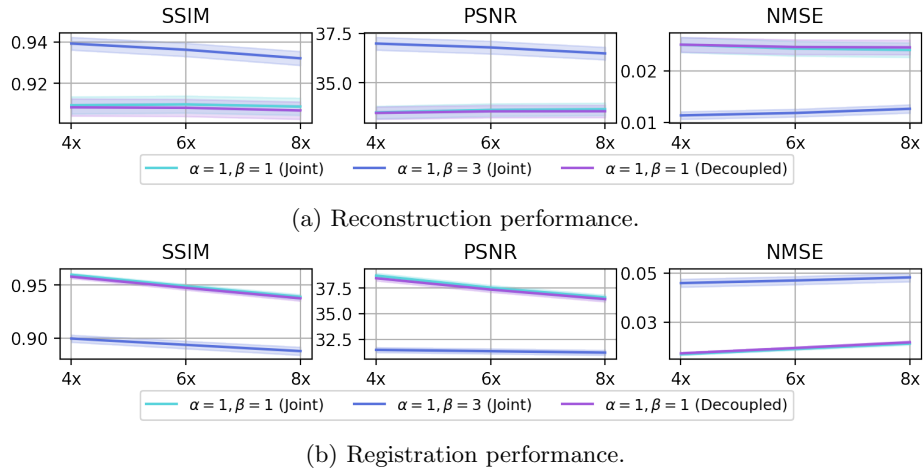


Fig. 9: Impact of joint vs decoupled training, and increased registration loss weight (cine dataset).

5 Discussion and Conclusion

In this work we present a novel pipeline integrating adaptive (under)sampling, reconstruction, and registration in an end-to-end framework for dynamic MRI. Our experiments provide a thorough evaluation of each component, on both in and out-of-distribution datasets, highlighting the flexibility and performance of this approach.

Our results show that our motion estimation module achieves strong registration performance, measured by registered moving image’s similarity to the reference, and provides efficient inference speeds compared to other considered deep learning and traditional methods.

Similarly, when testing an additional reconstruction network (VarNet), results indicated that our pipeline performed better with vSHARP as the reconstruction model, as evidenced by the registration outcomes.

While alternative hyperparameters for the registration component or utilizing different reconstruction algorithms might yield different outcomes, our aim is not to identify the optimal models but to underscore the modularity of our pipeline, allowing for interchangeable reconstruction or registration modules in a plug-and-play configuration.

Our evaluation of learned versus fixed sampling methods indicates that using an adaptive or optimized learned sampler leads to better registration field estimation than equidistant sampling schemes. This aligns with [61], where adaptive sampling also improved reconstruction quality over fixed schemes, although the difference between adaptive and optimized sampling remained minor here. Additionally, phase-specific sampling patterns, rather than unified, improved registration, while equispaced initialization did not enhance motion estimation, contrasting with its positive impact on reconstruction found in [61].

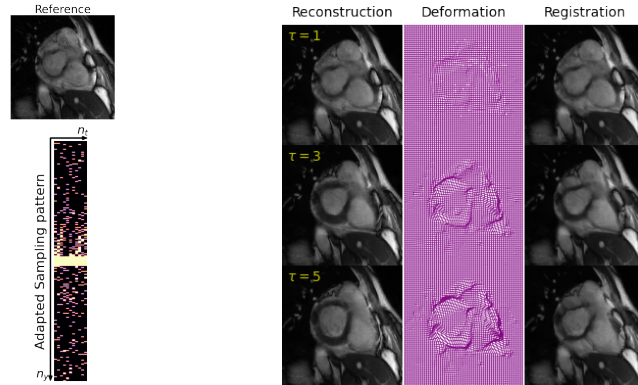
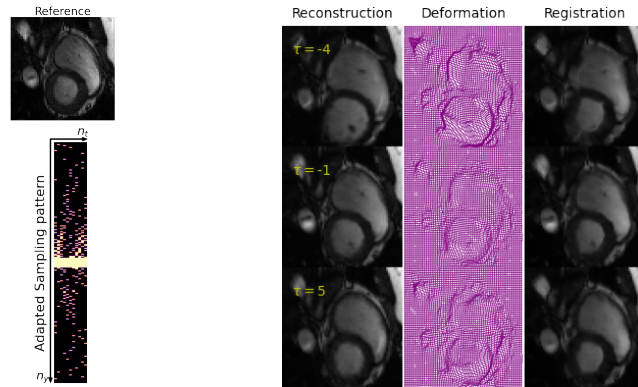
(a) Case I, $R = 6$.(b) Case II, $R = 8$.

Fig. 10: Example results for two cases, shown at various temporal frames (τ) relative to the reference image.

Finally, we compared joint versus decoupled training schemes. In the decoupled setup, task-specific losses were optimized by freezing the registration model weights during reconstruction loss computation, and vice versa. While joint optimization yielded only modest improvements over decoupled training, its value becomes clearer in our experiment with increased weighting on the registration loss. In this setting, prioritizing registration led to improved registration metrics despite a decline in reconstruction quality, highlighting how joint training allows flexible task prioritization. Future work could explore setting $\alpha = 0$, focusing exclusively on registration to evaluate its standalone impact.

Since we compared registered reconstructed moving images ($\hat{\mathbf{x}}_{\text{mov}}$) to the reference, our results reflect both registration and reconstruction quality. Evaluating motion estimation independently by comparing registered ground truth moving images (\mathbf{x}_{mov})-using the predicted deformation fields-to the reference

would provide a more objective assessment. Future research should also directly assess registration accuracy with relevant methods [45,36].

A limitation of our study is the reliance on fully sampled dynamic/moving k -space as ground truths, which are often unavailable due to motion constraints. Although self-supervised learning (SSL) methods exist for reconstruction [51,54,52], the adaptive sampling component requires access to a ground truth k -space. For the registration component, however, since it is trained in an unsupervised manner and only requires a fully sampled reference image, this issue is less problematic. Future work could explore SSL adaptations for the adaptive sampling component.

A further limitation is that our approach is two-dimensional, estimating motion between dynamic 2D (moving) slices and a reference 2D slice. A 3D approach could capture inter-slice correlations, though it would require a 4D (3D + time) reconstruction network, which would be computationally intensive for GPU memory during training (e.g., for back-propagation). Future work should consider exploring such a 3D approach.

This study marks the first application of an end-to-end, DL-based pipeline that jointly optimizes coil sensitivity estimation, adaptive sampling, reconstruction, and registration to enhance motion estimation between moving undersampled and reference images. The results suggest that each component contributes distinct benefits. Further research should investigate approaches that bypass reconstruction altogether, aiming to estimate motion directly from adaptively undersampled measurements for a more efficient workflow.

References

1. Adler, J., Öktem, O.: Learned primal-dual reconstruction. *IEEE transactions on medical imaging* **37**(6), 1322–1332 (2018)
2. Aggarwal, H.K., Mani, M.P., Jacob, M.: Modl: Model-based deep learning architecture for inverse problems. *IEEE transactions on medical imaging* **38**(2), 394–405 (2018)
3. Bahadir, C.D., Dalca, A.V., Sabuncu, M.R.: Learning-Based Optimization of the Under-Sampling Pattern in MRI, p. 780–792. Springer International Publishing (2019). https://doi.org/10.1007/978-3-030-20351-1_61
4. Bakker, T., Muckley, M.J., Romero-Soriano, A., Drozdal, M., Pineda, L.: On learning adaptive acquisition policies for undersampled multi-coil MRI reconstruction. In: *Medical Imaging with Deep Learning* (2022)
5. Balakrishnan, G., Zhao, A., Sabuncu, M.R., Gutttag, J., Dalca, A.V.: Voxelmorph: a learning framework for deformable medical image registration. *IEEE transactions on medical imaging* **38**(8), 1788–1800 (2019)
6. Beauferris, Y., Teuwen, J., Karkalousos, D., Moriakov, N., Caan, M., Yiasemis, G., Rodrigues, L., Lopes, A., Pedrini, H., Rittner, L., Dannecker, M., Studenyak, V., Gröger, F., Vyas, D., Faghih-Roohi, S., Kumar Jethi, A., Chandra Raju, J., Sivaprakasam, M., Lasby, M., Nogovitsyn, N., Loos, W., Frayne, R., Souza, R.: Multi-coil mri reconstruction challenge—assessing brain mri reconstruction models and their generalizability to varying coil configurations. *Frontiers in Neuroscience* **16** (2022). <https://doi.org/10.3389/fnins.2022>

- 919186, <https://www.frontiersin.org/journals/neuroscience/articles/10.3389/fnins.2022.919186>
7. Bengio, Y., Léonard, N., Courville, A.: Estimating or propagating gradients through stochastic neurons for conditional computation. arXiv preprint arXiv:1308.3432 (2013)
 8. Bertelsen, A., Bernchou, U., Schytte, T., Brink, C., Mahmood, F.: The effect of respiration-induced target motion on 3d magnetic resonance images used to guide radiotherapy. *Physics and Imaging in Radiation Oncology* **24**, 167–172 (2022)
 9. Chen, J., Frey, E.C., He, Y., Segars, W.P., Li, Y., Du, Y.: Transmorph: Transformer for unsupervised medical image registration. *Medical image analysis* **82**, 102615 (2022)
 10. Chen, X., Diaz-Pinto, A., Ravikumar, N., Frangi, A.F.: Deep learning in medical image registration. *Progress in Biomedical Engineering* **3**(1), 012003 (2021)
 11. Chen, Y., Schönlieb, C.B., Liò, P., Leiner, T., Dragotti, P.L., Wang, G., Rueckert, D., Firmin, D., Yang, G.: Ai-based reconstruction for fast mri—a systematic review and meta-analysis. *Proceedings of the IEEE* **110**(2), 224–245 (2022)
 12. Commowick, O., Arsigny, V., Isambert, A., Costa, J., Dhermain, F., Bidault, F., Bondiau, P.Y., Ayache, N., Malandain, G.: An efficient locally affine framework for the smooth registration of anatomical structures. *Medical Image Analysis* **12**(4), 427–441 (2008)
 13. Corona, V., Aviles-Rivero, A., Debroux, N., Le Guyader, C., Schönlieb, C.B.: Variational multi-task mri reconstruction: Joint reconstruction, registration and super-resolution. *Medical Image Analysis* **68**, 101941 (2021)
 14. Eo, T., Jun, Y., Kim, T., Jang, J., Lee, H.J., Hwang, D.: Kiki-net: cross-domain convolutional neural networks for reconstructing undersampled magnetic resonance images. *Magnetic resonance in medicine* **80**(5), 2188–2201 (2018)
 15. Gamper, U., Boesiger, P., Kozerke, S.: Compressed sensing in dynamic mri. *Magnetic Resonance in Medicine: An Official Journal of the International Society for Magnetic Resonance in Medicine* **59**(2), 365–373 (2008)
 16. Gautam, S., Li, A., Ravishankar, S.: Patient-adaptive and learned mri data under-sampling using neighborhood clustering (2024)
 17. Hammernik, K., Klatzer, T., Kobler, E., Recht, M.P., Sodickson, D.K., Pock, T., Knoll, F.: Learning a variational network for reconstruction of accelerated mri data. *Magnetic resonance in medicine* **79**(6), 3055–3071 (2018)
 18. Hering, A., Kuckertz, S., Heldmann, S., Heinrich, M.: Enhancing label-driven deep deformable image registration with local distance metrics for state-of-the-art cardiac motion tracking (2018), <https://arxiv.org/abs/1812.01859>
 19. Hunt, A., Hansen, V., Oelfke, U., Nill, S., Hafeez, S.: Adaptive radiotherapy enabled by mri guidance. *Clinical Oncology* **30**(11), 711–719 (2018). <https://doi.org/10.1016/j.clon.2018.08.001>, <https://www.sciencedirect.com/science/article/pii/S0936655518304084>, mRI and Radiotherapy
 20. Ismail, T.F., Strugnell, W., Coletti, C., Božić-Iven, M., Weingaertner, S., Hammernik, K., Correia, T., Kuestner, T.: Cardiac mr: from theory to practice. *Frontiers in cardiovascular medicine* **9**, 826283 (2022)
 21. Jaderberg, M., Simonyan, K., Zisserman, A., et al.: Spatial transformer networks. *Advances in neural information processing systems* **28** (2015)
 22. Khalil, A., Ng, S.C., Liew, Y.M., Lai, K.W.: An overview on image registration techniques for cardiac diagnosis and treatment. *Cardiology Research and Practice* **2018**, 1–15 (Aug 2018). <https://doi.org/10.1155/2018/1437125>, <http://dx.doi.org/10.1155/2018/1437125>

23. Knoll, F., Murrell, T., Sriram, A., Yakubova, N., Zbontar, J., Rabbat, M., Defazio, A., Muckley, M.J., Sodickson, D.K., Zitnick, C.L., et al.: Advancing machine learning for mr image reconstruction with an open competition: Overview of the 2019 fastmri challenge. *Magnetic resonance in medicine* **84**(6), 3054–3070 (2020)
24. Kostelec, P.J., Periaswamy, S.: Image registration for mri. *Modern signal processing* **46**, 161–184 (2003)
25. Le Besnerais, G., Champagnat, F.: Dense optical flow by iterative local window registration. In: *IEEE International Conference on Image Processing 2005*. vol. 1, pp. I–137 (2005). <https://doi.org/10.1109/ICIP.2005.1529706>
26. Liu, Z., Lin, Y., Cao, Y., Hu, H., Wei, Y., Zhang, Z., Lin, S., Guo, B.: Swin transformer: Hierarchical vision transformer using shifted windows. In: *Proceedings of the IEEE/CVF international conference on computer vision*. pp. 10012–10022 (2021)
27. Lønning, K., Caan, M.W., Nowee, M.E., Sonke, J.J.: Dynamic recurrent inference machines for accelerated mri-guided radiotherapy of the liver. *Computerized Medical Imaging and Graphics* **113**, 102348 (2024)
28. Lowekamp, B.C., Chen, D.T., Ibanez, L., Blezek, D.: The design of simpleitk. *Frontiers in Neuroinformatics* **7** (2013). <https://doi.org/10.3389/fninf.2013.00045>, <https://www.frontiersin.org/journals/neuroinformatics/articles/10.3389/fninf.2013.00045>
29. Lustig, M., Donoho, D.L., Santos, J.M., Pauly, J.M.: Compressed sensing mri. *IEEE signal processing magazine* **25**(2), 72–82 (2008)
30. Lyu, J., Qin, C., Wang, S., Wang, F., Li, Y., Wang, Z., Guo, K., Ouyang, C., Tänzer, M., Liu, M., Sun, L., Sun, M., Li, Q., Shi, Z., Hua, S., Li, H., Chen, Z.: The state-of-the-art in cardiac mri reconstruction: Results of the cmrxrecon challenge in miccai 2023 (2024), <https://arxiv.org/abs/2404.01082>
31. Mada, R.O., Lysyansky, P., Daraban, A.M., Duchenne, J., Voigt, J.U.: How to define end-diastole and end-systole?: Impact of timing on strain measurements. *JACC: Cardiovascular Imaging* **8**(2), 148–157 (2015). <https://doi.org/https://doi.org/10.1016/j.jcmg.2014.10.010>, <https://www.sciencedirect.com/science/article/pii/S1936878X1400936X>
32. Oscanoa, J.A., Middione, M.J., Alkan, C., Yurt, M., Loecher, M., Vasanawala, S.S., Ennis, D.B.: Deep learning-based reconstruction for cardiac mri: A review. *Bioengineering* **10**(3) (2023). <https://doi.org/10.3390/bioengineering10030334>, <https://www.mdpi.com/2306-5354/10/3/334>
33. Pal, A., Rathi, Y.: A review and experimental evaluation of deep learning methods for mri reconstruction. *The journal of machine learning for biomedical imaging* **1** (2022)
34. Paszke, A., Gross, S., Massa, F., Lerer, A., Bradbury, J., Chanan, G., Killeen, T., Lin, Z., Gimelshein, N., Antiga, L., et al.: Pytorch: An imperative style, high-performance deep learning library. *Advances in neural information processing systems* **32** (2019)
35. Ronneberger, O., Fischer, P., Brox, T.: U-net: Convolutional networks for biomedical image segmentation. In: *Medical image computing and computer-assisted intervention—MICCAI 2015: 18th international conference, Munich, Germany, October 5–9, 2015, proceedings, part III 18*. pp. 234–241. Springer (2015)
36. Saleh, Z.H., Apte, A.P., Sharp, G.C., Shusharina, N.P., Wang, Y., Veeraraghavan, H., Thor, M., Muren, L.P., Rao, S.S., Lee, N.Y., et al.: The distance discordance metric—a novel approach to quantifying spatial uncertainties in intra-and inter-patient deformable image registration. *Physics in Medicine & Biology* **59**(3), 733 (2014)

37. Shannon, C.: Communication in the presence of noise. *Proceedings of the IRE* **37**(1), 10–21 (1949). <https://doi.org/10.1109/JRPROC.1949.232969>
38. Shor, T.: Multi PILOT: Feasible learned multiple acquisition trajectories for dynamic MRI. In: *Medical Imaging with Deep Learning* (2023)
39. Sriram, A., Zbontar, J., Murrell, T., Defazio, A., Zitnick, C.L., Yakubova, N., Knoll, F., Johnson, P.: End-to-end variational networks for accelerated mri reconstruction. In: *Medical Image Computing and Computer Assisted Intervention—MICCAI 2020: 23rd International Conference, Lima, Peru, October 4–8, 2020, Proceedings, Part II* 23. pp. 64–73. Springer (2020)
40. Sun, S., Han, K., You, C., Tang, H., Kong, D., Naushad, J., Yan, X., Ma, H., Khosravi, P., Duncan, J.S., et al.: Medical image registration via neural fields. *Medical Image Analysis* **97**, 103249 (2024)
41. Terpstra, M.L., Maspero, M., Bruijnen, T., Verhoeff, J.J., Lagendijk, J.J., van den Berg, C.A.: Real-time 3d motion estimation from undersampled mri using multi-resolution neural networks. *Medical physics* **48**(11), 6597–6613 (2021)
42. Terpstra, M.L., Maspero, M., Sbrizzi, A., van den Berg, C.A.: \perp -loss: A symmetric loss function for magnetic resonance imaging reconstruction and image registration with deep learning. *Medical Image Analysis* **80**, 102509 (2022). <https://doi.org/https://doi.org/10.1016/j.media.2022.102509>, <https://www.sciencedirect.com/science/article/pii/S1361841522001566>
43. Thirion, J.P.: Image matching as a diffusion process: an analogy with maxwell’s demons. *Medical image analysis* **2**(3), 243–260 (1998)
44. Tsao, J., Boesiger, P., Pruessmann, K.P.: k-t blast and k-t sense: dynamic mri with high frame rate exploiting spatiotemporal correlations. *Magnetic Resonance in Medicine: An Official Journal of the International Society for Magnetic Resonance in Medicine* **50**(5), 1031–1042 (2003)
45. Vandemeulebroucke, J., Sarrut, D., Clarysse, P., et al.: The popi-model, a point-validated pixel-based breathing thorax model. In: *XVth international conference on the use of computers in radiation therapy (ICCR)*. vol. 2, pp. 195–199 (2007)
46. Waddington, D.E., Hindley, N., Koonjoo, N., Chiu, C., Reynolds, T., Liu, P.Z., Zhu, B., Bhutto, D., Paganelli, C., Keall, P.J., et al.: On real-time image reconstruction with neural networks for mri-guided radiotherapy. *arXiv preprint arXiv:2202.05267* (2022)
47. Van der Walt, S., Schönberger, J.L., Nunez-Iglesias, J., Boulogne, F., Warner, J.D., Yager, N., Gouillart, E., Yu, T.: scikit-image: image processing in python. *PeerJ* **2**, e453 (2014)
48. Wang, C., Li, Y., Lv, J., Jin, J., Hu, X., Kuang, X., Chen, W., Wang, H.: Recommendation for cardiac magnetic resonance imaging-based phenotypic study: Imaging part. *Phenomics* **1**(4), 151–170 (Jul 2021). <https://doi.org/10.1007/s43657-021-00018-x>
49. Wang, C., et al.: Cmrrecon: An open cardiac mri dataset for the competition of accelerated image reconstruction (2023). <https://doi.org/10.48550/ARXIV.2309.10836>
50. Wang, Z., Wang, F., Qin, C., Lyu, J., Cheng, O., Wang, S., Li, Y., Yu, M., Zhang, H., Guo, K., Shi, Z., Li, Q., Xu, Z., Zhang, Y., Li, H., Hua, S., Chen, B., Sun, L., Sun, M., Li, Q., Chu, Y.H., Bai, W., Qin, J., Zhuang, X., Prieto, C., Young, A., Markl, M., Wang, H., Wu, L., Yang, G., Qu, X., Wang, C.: Cmrrecon2024: A multi-modality, multi-view k-space dataset boosting universal machine learning for accelerated cardiac mri (2024), <https://arxiv.org/abs/2406.19043>

51. Yaman, B., Hosseini, S.A.H., Moeller, S., Ellermann, J., Uğurbil, K., Akçakaya, M.: Self-supervised learning of physics-guided reconstruction neural networks without fully sampled reference data. *Magnetic resonance in medicine* **84**(6), 3172–3191 (2020)
52. Yan, Y., Yang, T., Zhao, X., Jiao, C., Yang, A., Miao, J.: Dc-siamnet: Deep contrastive siamese network for self-supervised mri reconstruction. *Computers in Biology and Medicine* **167**, 107619 (2023)
53. Yang, F., Xue, Z., Lu, H., Xu, J., Chen, H., Chen, Z., Emu, Y., Aburas, A., Gao, J., Gao, C., et al.: Robust fast inter-bin image registration for undersampled coronary mri based on a learned motion prior. *IEEE Transactions on Biomedical Engineering* (2024)
54. Yiasemis, G., Moriakov, N., Sánchez, C.I., Sonke, J.J., Teuwen, J.: Jssl: Joint supervised and self-supervised learning for mri reconstruction. *arXiv preprint arXiv:2311.15856* (2023)
55. Yiasemis, G., Moriakov, N., Sonke, J.J., Teuwen, J.: Deep cardiac mri reconstruction with admm. In: *International Workshop on Statistical Atlases and Computational Models of the Heart*. pp. 479–490. Springer (2023)
56. Yiasemis, G., Moriakov, N., Sonke, J.J., Teuwen, J.: Deep multi-contrast cardiac mri reconstruction via vsharp with auxiliary refinement network. *arXiv preprint arXiv:2411.01291* (2024)
57. Yiasemis, G., Moriakov, N., Sonke, J.J., Teuwen, J.: Deep multi-contrast cardiac mri reconstruction via vsharp with auxiliary refinement network (2024), <https://arxiv.org/abs/2411.01291>
58. Yiasemis, G., Moriakov, N., Sonke, J.J., Teuwen, J.: vsharp: variable splitting half-quadratic admm algorithm for reconstruction of inverse-problems. *Magnetic Resonance Imaging* p. 110266 (2024)
59. Yiasemis, G., Sánchez, C.I., Sonke, J.J., Teuwen, J.: On retrospective k-space subsampling schemes for deep mri reconstruction. *Magnetic Resonance Imaging* **107**, 33–46 (2024)
60. Yiasemis, G., Sonke, J.J., Sánchez, C., Teuwen, J.: Recurrent variational network: a deep learning inverse problem solver applied to the task of accelerated mri reconstruction. In: *Proceedings of the IEEE/CVF conference on computer vision and pattern recognition*. pp. 732–741 (2022)
61. Yiasemis, G., Sonke, J.J., Teuwen, J.: End-to-end adaptive dynamic subsampling and reconstruction for cardiac mri (2024), <https://arxiv.org/abs/2403.10346>
62. Yin, T., Wu, Z., Sun, H., Dalca, A.V., Yue, Y., Bouman, K.L.: End-to-end sequential sampling and reconstruction for mri. *arXiv preprint arXiv:2105.06460* (2021)
63. Yoo, J., Jin, K.H., Gupta, H., Yerly, J., Stuber, M., Unser, M.: Time-dependent deep image prior for dynamic mri. *IEEE Transactions on Medical Imaging* **40**(12), 3337–3348 (2021)
64. Zach, C., Pock, T., Bischof, H.: A duality based approach for realtime tv-l1 optical flow. In: *Hamprecht, F.A., Schnörr, C., Jähne, B. (eds.) Pattern Recognition*. pp. 214–223. Springer Berlin Heidelberg, Berlin, Heidelberg (2007)
65. Zhang, J., Zhang, H., Wang, A., Zhang, Q., Sabuncu, M., Spincemaille, P., Nguyen, T.D., Wang, Y.: Extending loupe for k-space under-sampling pattern optimization in multi-coil mri (2020)
66. Zhang, Z.: Improved adam optimizer for deep neural networks. In: *2018 IEEE/ACM 26th international symposium on quality of service (IWQoS)*. pp. 1–2. Ieee (2018)

Deep End-to-end Adaptive k-Space Sampling, Reconstruction, and Registration for Dynamic MRI - Supplementary Material

A Methods - Additional Information

A.1 Sensitivity Profile Network

As detailed in the main text and following [39], the sensitivity profiles for the multi-coil data, denoted as $\tilde{\mathbf{S}} \in \mathbb{C}^{n^2 \times n_c \times n_t}$, are initially estimated using the fully sampled central region of the k -space, $\tilde{\mathbf{y}}_{\text{mov}}^{\text{M}^{\text{acs}}}$, corresponding to the low-frequency autocalibration signal. This estimation is computed as:

$$\tilde{\mathbf{S}}_{\tau}^k = \mathcal{F}^{-1}((\tilde{\mathbf{y}}_{\text{mov}}^{\text{M}^{\text{acs}}})_{\cdot, k, \tau}) \oslash \text{RSS}\left(\mathcal{F}^{-1}((\tilde{\mathbf{y}}_{\text{mov}}^{\text{M}^{\text{acs}}})_{\cdot, 1, \tau}), \dots, \mathcal{F}^{-1}((\tilde{\mathbf{y}}_{\text{mov}}^{\text{M}^{\text{acs}}})_{\cdot, n_c, \tau})\right), \quad (\text{A1})$$

where \oslash represents element-wise (Hadamard) division, and $\text{RSS}(\cdot)$ computes the root sum of squares.

These initial sensitivity estimates, consistent with the methodology in [39], are further refined using a deep learning-based model. Specifically, a two-dimensional U-Net [35], denoted as \mathcal{S}_{σ} , is employed to enhance the sensitivity profiles:

$$\mathbf{S}_{\tau}^k := \mathcal{S}_{\sigma}(\tilde{\mathbf{S}}_{\tau}^k), \quad \tau = 1, \dots, n_t, \quad k = 1, \dots, n_c. \quad (\text{A2})$$

The refined sensitivity profiles are subsequently normalized to satisfy:

$$\sum_{k=1}^{n_c} (\mathbf{S}_{\tau}^k)^* \mathbf{S}_{\tau}^k = \mathbf{I}_n \in \mathbb{R}^{n \times n}. \quad (\text{A3})$$

A.2 Reconstruction Network - vSHARP

In our original pipeline, we employed the variable Splitting Half-quadratic ADMM algorithm for Reconstruction of inverse Problems (vSHARP) as the reconstruction network. vSHARP is an unrolled, physics-guided deep learning framework [58], which has demonstrated effectiveness in accelerated dynamic cardiac MRI reconstruction. Notably, it was among the winning solutions of the CMRxRecon 2023 and 2024 challenges [55,57]. The vSHARP algorithm leverages the half-quadratic variable splitting technique for the optimization problem defined in (6), introducing an auxiliary variable \mathbf{z} as follows:

$$\min_{\mathbf{x}', \mathbf{z} \in \mathbb{C}^{n \times n_t}} \frac{1}{2} \sum_{\tau=1}^{n_t} \left\| \mathcal{T}_{\mathbf{M}_{\tau}, \mathbf{C}_{\tau}}(\mathbf{x}'_{\cdot, \tau}) - \tilde{\mathbf{y}}_{\cdot, \tau}^{\text{M}} \right\|_2^2 + \mathcal{H}(\mathbf{z}) \quad \text{subject to } \mathbf{x}' = \mathbf{z}. \quad (\text{A4})$$

Equation (A4) is then unrolled over T iterations using the Alternating Direction Method of Multipliers (ADMM), comprising three main steps at each

iteration: **(i)** denoising to refine the auxiliary variable \mathbf{z} , **(ii)** data consistency for the target image \mathbf{x} , and **(iii)** updating the Lagrange multipliers \mathbf{m} introduced by ADMM:

$$\mathbf{z}^{t+1} = \underset{\mathbf{z} \in \mathbb{C}^{n \times n_t}}{\operatorname{argmin}} \mathcal{H}(\mathbf{z}) + \frac{\lambda^{t+1}}{2} \left\| \mathbf{x}^t - \mathbf{z} + \frac{\mathbf{m}^t}{\lambda^{t+1}} \right\|_2^2 := \mathcal{D}_{\boldsymbol{\theta}^{t+1}} \left(\mathbf{z}^t, \mathbf{x}^t, \frac{\mathbf{m}^t}{\lambda^{t+1}} \right), \quad (\text{A5a})$$

$$\mathbf{x}^{t+1} = \underset{\mathbf{x}' \in \mathbb{C}^{n \times n_t}}{\operatorname{argmin}} \frac{1}{2} \sum_{\tau=1}^{n_t} \left\| \mathcal{T}_{\mathbf{M}_\tau, \mathbf{C}_\tau}(\mathbf{x}'_{\cdot, \tau}) - \tilde{\mathbf{y}}_{\cdot, \tau}^{\mathbf{M}} \right\|_2^2 + \lambda^{t+1} \left\| \mathbf{x}' - \mathbf{z}^{t+1} + \frac{\mathbf{m}^t}{\lambda^{t+1}} \right\|_2^2, \quad (\text{A5b})$$

$$\mathbf{m}^{t+1} = \mathbf{m}^t + \lambda^{t+1} (\mathbf{x}^{t+1} - \mathbf{z}^{t+1}). \quad (\text{A5c})$$

In (A5a), $\mathcal{D}_{\boldsymbol{\theta}^{t+1}}$ denotes a convolutional DL-based image denoiser with trainable parameters $\boldsymbol{\theta}^{t+1}$, and λ^{t+1} is a trainable learning rate. At each iteration, $\mathcal{D}_{\boldsymbol{\theta}^{t+1}}$ processes the previous estimates of the three variables, yielding an updated estimate for \mathbf{z} . Equation A5b is numerically optimized using a differentiable gradient descent scheme unrolled over $T_{\mathbf{x}}$ iterations. The update in (A5c) involves a straightforward calculation. The initial estimates for \mathbf{x} and \mathbf{z} are defined as follows:

$$\mathbf{x}_\tau^0, \mathbf{z}_\tau^0 = \mathcal{R}_{\mathbf{S}_\tau} \circ \mathcal{F}^{-1}(\tilde{\mathbf{y}}_\tau^{\mathbf{M}}). \quad (\text{A6})$$

For \mathbf{m}^0 , vSHARP employs a trainable network $\mathcal{I}^{\boldsymbol{\theta}^x}$ initialized using \mathbf{x}_τ^0 :

$$\mathbf{m}^0 := \mathcal{I}^{\boldsymbol{\theta}^x}(\mathbf{x}^0). \quad (\text{A7})$$

Accordingly, the trainable parameters of the vSHARP reconstruction model are defined as:

$$\boldsymbol{\theta} = \left\{ \boldsymbol{\theta}^1, \dots, \boldsymbol{\theta}^T, \boldsymbol{\theta}^x, \lambda^1, \dots, \lambda^T \right\}. \quad (\text{A8})$$

B Experiments - Additional Information

B.1 Datasets

As outlined in the main text, the cardiac cine dataset from the CMRxRecon 2023 challenge [49,48] was used. This dataset includes 471 4D cardiac k -space scans, resulting in 3,185 2D dynamic sequences. It features short- and long-axis views across two-, three-, and four-chamber configurations. Each scan is fully sampled, ECG-triggered, and acquired using multi-coil ($n_c = 10$) setups. The dataset spans 3–12 dynamic slices per case, with each cardiac cycle divided into 12 temporal frames. The dataset was split into 251, 100, and 100 4D volumes for training, validation, and testing, respectively (comprising 1,710, 731, and 744 dynamic slices).

For external validation, the aorta dataset from the CMRxRecon 2024 challenge [50] was employed. This dataset also contains fully sampled, ECG-triggered multi-coil acquisitions segmented into 12 temporal frames. Transverse and sagittal views of the aorta were provided, with the subset used for inference consisting of 111 scans and 883 dynamic slices.

Figure 11 illustrates representative fully sampled reconstructed images from each dataset, showcasing the diversity of anatomical views.

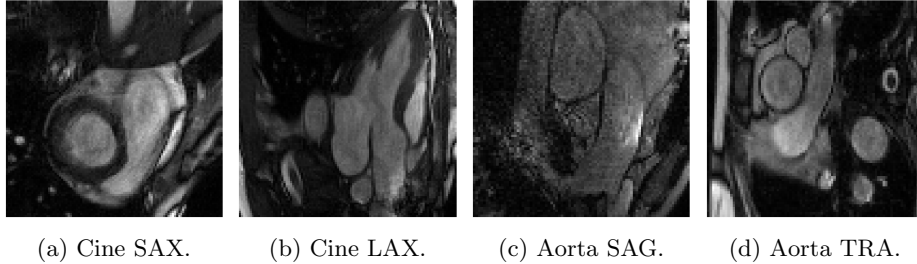


Fig. 11: Representative fully sampled images across cardiac phases and views from each dataset.

B.2 Undersampling

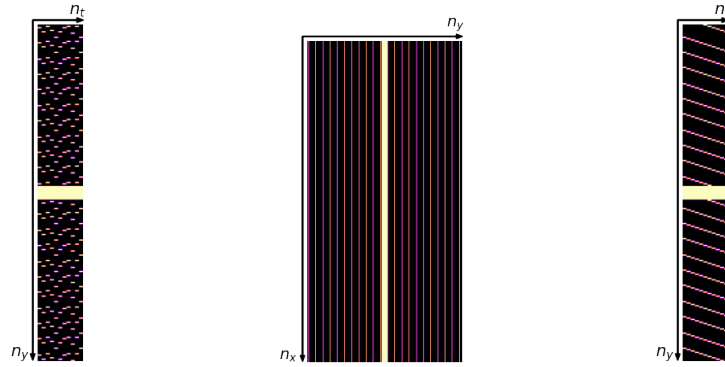
Learned Sampling Experiments utilized 1D line (rectilinear) sampling patterns, retaining certain lines in the phase-encoding direction of the Cartesian grid. For learned sampling patterns (adaptive or optimized), data were subsampled using the following strategies:

1. Autocalibration Signal (ACS): The central k -space region was retained, covering 4% of the fully sampled data.
2. Equispaced Sampling: Applied with a target acceleration factor of $(R - 4) \times$, where R is the target acceleration. ACS measurements (4% of the fully sampled data) were included in this sampling pattern.

For adaptive sampling, the initial undersampled data informed the acquisition of additional data at the target acceleration factor. In optimized sampling experiments, initialization was not strictly required but ensured inclusion of ACS data.

Fixed Sampling For fixed (non-learned) sampling, we applied two distinct strategies:

1. Equispaced: Lines were evenly spaced to achieve the target acceleration, with the central offset randomized during training and fixed during inference. Separate patterns were used for phase-specific experiments, while a unified pattern was applied across all phases in unified experiments. Examples are shown in Figure 12a and Figure 12b.



(a) Phase-specific equispaced sampling pattern. Each time-step represents a scheme per each phase. Each point represents a line along the n_x direction.
 (b) Unified equispaced sampling pattern.
 (c) kt -Equispaced sampling pattern. Each time-step represents a scheme per each phase. Each point represents a line along the n_x direction.

Fig. 12: Representative examples of (fixed) sampling patterns.

2. kt -Equispaced: Used exclusively in phase-specific experiments, this strategy followed the method in [44], where equispaced sampling was performed per phase with temporal interleaving along the time dimension. An example of this pattern is presented in Figure 12c.

B.3 Evaluation Metrics

Assume $\mathbf{f}, \mathbf{d} \in \mathbb{R}^n$, where \mathbf{f} denotes a ground truth image and \mathbf{d} a prediction. Then the evaluation metrics we used are defined as follows:

- Structural Similarity Index Measure (SSIM)

$$\text{SSIM}(\mathbf{f}, \mathbf{d}) = \frac{1}{N} \sum_{i=1}^N \frac{(2\mu_{\mathbf{f}_i}\mu_{\mathbf{d}_i} + c_1)(2\sigma_{\mathbf{f}_i\mathbf{d}_i} + c_2)}{(\mu_{\mathbf{f}_i}^2 + \mu_{\mathbf{d}_i}^2 + c_1)(\sigma_{\mathbf{f}_i}^2 + \sigma_{\mathbf{d}_i}^2 + c_2)}, \quad (\text{B1})$$

where $\mathbf{f}_i, \mathbf{d}_i, i = 1, \dots, N$ represent 7×7 square windows of \mathbf{f}, \mathbf{d} , respectively, and $c_1 = 0.01, c_2 = 0.03$. Additionally, $\mu_{\mathbf{f}_i}, \mu_{\mathbf{d}_i}$ denote the means of each window, $\sigma_{\mathbf{f}_i}$ and $\sigma_{\mathbf{d}_i}$ represent the corresponding standard deviations. Lastly, $\sigma_{\mathbf{f}_i\mathbf{d}_i}$ represents the covariance between \mathbf{f}_i and \mathbf{d}_i .

- Peak signal-to-noise ratio (PSNR)

$$\text{PSNR}(\mathbf{f}, \mathbf{d}) = 20 \log_{10} \left(\frac{\max(\mathbf{f})}{\sqrt{\frac{1}{n} \sum_i^n (\mathbf{f}_i - \mathbf{d}_i)^2}} \right). \quad (\text{B2})$$

- Normalized Mean Squared Error (NMSE)

$$\text{NMSE}(\mathbf{f}, \mathbf{d}) = \frac{\|\mathbf{f} - \mathbf{d}\|_2^2}{\|\mathbf{f}\|_2^2} = \frac{\sum_{i=1}^n (\mathbf{f}_i - \mathbf{d}_i)^2}{\sum_{i=1}^n \mathbf{f}_i^2}. \quad (\text{B3})$$

B.4 Data Preprocessing and Postprocessing

Zero-padding Each 2D sequence comprised $n_t + 1 = 12$ cardiac cycle segments, $n_c = 10$ coils, and spatial dimensions varying between $n'_x = \{448, 512\}$ and $n'_y = \{132, 162, 168, 204, 246\}$ for the cine dataset, and $n'_x = 416$ and $n'_y = 168$ for the aorta dataset. Here, n'_x, n'_y represent the pre-padding shapes.

To accommodate the fixed input size required by the MLP component of the adaptive sampling module [61], data were zero-padded to the largest spatial dimensions, $(n_x, n_y) = (512, 246)$. Specifically, fully sampled k -space data were transformed to the image domain using the inverse FFT, zero-padded in the image domain, and projected back to k -space using the FFT.

Normalization Data were normalized using the 99.5th percentile of the flattened magnitude of the autocalibration signal k -space for each moving sequence:

$$s = \text{quantile}_{99.5} \left(\text{flatten}(|\mathbf{y}_{\text{mov}}^{\text{acs}}|) \right).$$

Postprocessing Cropping Registered data were evaluated on a center-cropped region (in the image domain) of size $(n'_x/3, n'_y/2)$, focusing on the region of interest (cardiac or aorta) as specified by the CMRxRecon challenge organizers.

B.5 Hyperparameter Choices

Warping Transform The warping transform is implemented in PyTorch [34] to ensure differentiability, following the spatial transformer framework described in the literature [21,5]. More specifically, the aim is to deform an input image I based on a displacement field \mathbf{v} , yielding a warped image I' . The process begins by integrating the displacement field \mathbf{v} over two steps using the scaling and squaring method. Mathematically, this computes $\mathbf{v}_{\text{integrated}} = \mathbf{v} + \mathbf{v} \circ \mathbf{v} + \dots$, where \circ denotes the composition of displacement fields. The integrated field defines a smooth transformation that is used to update spatial coordinates, ensuring the motion is captured accurately. The warped image is computed as $I'(\mathbf{x}) = I(\mathbf{x} + \mathbf{v}_{\text{integrated}}(\mathbf{x}))$, where \mathbf{x} represents pixel coordinates. The method also normalizes the transformed grid to the range $[-1, 1]$ to match the input tensor’s dimensions, applies bilinear sampling for smooth interpolation, and uses a binary mask to account for invalid or out-of-bound regions, ensuring the transformation is robust and accurate.

Registration Comparisons We evaluated multiple registration approaches, each configured with specific hyperparameters:

1. Voxelmorph with a 2D U-Net architecture comprising 4 scales with filter sizes of 16, 32, 64, and 128 was employed. For each moving (dynamic) image, we performed a forward pass for each temporal phase along with the reference image, consistent with the original implementation in [5].image.

2. Transmorph with a vision transformer model (ViT) inspired by the Swin Transformer [26], configured with a patch size of 10×10 , an embedding dimension of 64, 8 layers, and 9 attention heads. The setup also includes Global Position-Sensitive Attention (GPSA) intervals and locality strength to focus on spatial regions. Each moving image phase is processed with the reference image during the forward pass, adhering to the approach described in [9].
3. Our proposed registration model using a larger U-Net with enhanced capacity, featuring four scales with 32, 64, 128, and 252 filters at each scale.
4. Iterative Lucas-Kanade (ILK) optical flow method from `scikit-image`, configured with a radius of 5, 3 warp iterations, prefiltering enabled, and without Gaussian smoothing. All other parameters are based on the default settings of the `scikit-image` in https://scikit-image.org/docs/stable/api/skimage.registration.html#skimage.registration.optical_flow_ilk.
5. Total Variation L_1 optical flow method from `scikit-image`, configured with an attachment weight of 15, tightness parameter of 0.3, 3 warp iterations, 5 main iterations, and a tolerance of 1×10^{-2} . All other parameters are based on the default settings of the `scikit-image` in https://scikit-image.org/docs/stable/api/skimage.registration.html#skimage.registration.optical_flow_tv11.
6. Demons registration method configured with 10 iterations, a Gaussian smoothing standard deviation of 1.0, and smoothing applied to the displacement field, following the standard settings of the SimpleITK Demons algorithm. See https://simpleitk.org/doxygen/latest/html/classitk_1_1simple_1_1DemonsRegistrationFilter.html.

C Additional Results

C.1 Additional Tables

Model	Reconstruction Sampling Type	Sampling Initialization	Registration Module	Joint Loss	Loss				Weights						
					4×		6×		8×		8×				
					SSIM (↑)	PSNR (↑)	NMSE (↓)	SSIM (↑)	PSNR (↑)	NMSE (↓)	SSIM (↑)	PSNR (↑)	NMSE (↓)	SSIM (↑)	PSNR (↑)
α	β														
vSHARP	Adaptive	×	Learned	✓	1	1	0.907 ± 0.041	33.57 ± 3.19	0.025 ± 0.015	0.910 ± 0.041	33.63 ± 3.18	0.024 ± 0.014	0.909 ± 0.042	33.67 ± 3.16	0.024 ± 0.014
vSHARP	Adaptive	×	Learned (L)	✓	1	1	0.905 ± 0.041	33.43 ± 3.14	0.025 ± 0.015	0.909 ± 0.041	33.58 ± 3.13	0.024 ± 0.014	0.909 ± 0.041	33.64 ± 3.12	0.024 ± 0.014
vSHARP	Adaptive	×	Voxchmorph	✓	1	1	0.889 ± 0.046	32.16 ± 2.92	0.033 ± 0.017	0.886 ± 0.047	32.13 ± 2.91	0.033 ± 0.017	0.882 ± 0.048	32.04 ± 2.89	0.034 ± 0.017
vSHARP	Adaptive	×	Transformorph	✓	1	1	0.886 ± 0.046	31.37 ± 3.02	0.040 ± 0.022	0.886 ± 0.046	31.47 ± 3.00	0.039 ± 0.022	0.886 ± 0.046	31.50 ± 2.95	0.039 ± 0.021
vSHARP	Adaptive	×	Learned	✓	1	3	0.939 ± 0.031	36.99 ± 3.26	0.011 ± 0.007	0.936 ± 0.032	36.79 ± 3.22	0.012 ± 0.008	0.932 ± 0.034	36.49 ± 3.19	0.013 ± 0.008
vSHARP	Adaptive	×	Learned	×	1	1	0.908 ± 0.041	33.48 ± 3.14	0.025 ± 0.014	0.908 ± 0.042	33.56 ± 3.14	0.025 ± 0.014	0.907 ± 0.042	33.56 ± 3.12	0.025 ± 0.014
vSHARP	Adaptive	✓	Learned	✓	1	1	0.907 ± 0.042	33.33 ± 3.15	0.026 ± 0.015	0.907 ± 0.042	33.45 ± 3.15	0.025 ± 0.015	0.906 ± 0.042	33.47 ± 3.12	0.025 ± 0.015
vSHARP	Adaptive	✓	Learned	✓	1	1	0.905 ± 0.043	32.95 ± 3.15	0.028 ± 0.017	0.906 ± 0.043	33.08 ± 3.15	0.028 ± 0.016	0.904 ± 0.043	33.13 ± 3.12	0.027 ± 0.016
vSHARP	Equi	NA	Learned	✓	1	1	0.897 ± 0.045	32.47 ± 3.08	0.031 ± 0.018	0.898 ± 0.045	32.65 ± 3.08	0.030 ± 0.017	0.893 ± 0.046	32.61 ± 3.00	0.030 ± 0.017
vSHARP	Equi	NA	Learned	×	1	1	0.896 ± 0.045	32.31 ± 3.07	0.033 ± 0.019	0.895 ± 0.046	32.44 ± 3.07	0.032 ± 0.018	0.890 ± 0.047	32.38 ± 2.99	0.032 ± 0.018
vSHARP	It-equi	NA	Learned	✓	1	1	0.899 ± 0.045	32.59 ± 3.14	0.031 ± 0.018	0.900 ± 0.045	32.77 ± 3.14	0.030 ± 0.017	0.893 ± 0.047	32.73 ± 3.09	0.030 ± 0.017
vSHARP	It-equi	NA	Learned	×	1	1	0.895 ± 0.046	32.24 ± 3.10	0.033 ± 0.019	0.896 ± 0.046	32.40 ± 3.09	0.032 ± 0.018	0.890 ± 0.048	32.37 ± 3.05	0.032 ± 0.018
vSHARP	Optimized	×	Learned	✓	1	1	0.912 ± 0.040	33.76 ± 3.14	0.023 ± 0.013	0.912 ± 0.040	33.87 ± 3.14	0.023 ± 0.013	0.910 ± 0.041	33.87 ± 3.11	0.023 ± 0.013
VacNet	Adaptive	×	Learned	✓	1	1	0.886 ± 0.052	33.15 ± 2.97	0.026 ± 0.013	0.870 ± 0.056	32.44 ± 2.87	0.030 ± 0.015	0.863 ± 0.055	32.15 ± 2.73	0.032 ± 0.015
vSHARP	Adaptive	×	OFILK	NA	1	NA	0.890 ± 0.044	32.20 ± 2.89	0.033 ± 0.018	0.889 ± 0.044	32.21 ± 2.89	0.033 ± 0.018	0.887 ± 0.045	32.17 ± 2.87	0.033 ± 0.018
vSHARP	Adaptive	×	OFTVLI	NA	1	NA	0.893 ± 0.042	30.69 ± 3.08	0.049 ± 0.030	0.892 ± 0.042	30.66 ± 3.06	0.049 ± 0.030	0.891 ± 0.042	30.63 ± 3.05	0.049 ± 0.030
vSHARP	Adaptive	×	DEMONS	NA	1	NA	0.892 ± 0.044	30.77 ± 2.87	0.045 ± 0.023	0.891 ± 0.045	30.80 ± 2.86	0.045 ± 0.023	0.890 ± 0.045	30.82 ± 2.85	0.045 ± 0.023
vSHARP	Equi	NA	OFILK	NA	1	NA	0.888 ± 0.045	32.14 ± 2.89	0.033 ± 0.018	0.886 ± 0.045	32.14 ± 2.88	0.033 ± 0.018	0.880 ± 0.048	32.01 ± 2.84	0.034 ± 0.018
vSHARP	Equi	NA	OFTVLI	NA	1	NA	0.891 ± 0.042	30.58 ± 3.09	0.050 ± 0.031	0.889 ± 0.043	30.55 ± 3.07	0.050 ± 0.031	0.883 ± 0.045	30.37 ± 3.01	0.052 ± 0.032
vSHARP	Equi	NA	DEMONS	NA	1	NA	0.890 ± 0.045	30.74 ± 2.88	0.046 ± 0.023	0.889 ± 0.046	30.78 ± 2.87	0.045 ± 0.023	0.884 ± 0.047	30.79 ± 2.85	0.045 ± 0.023
vSHARP	It-equi	NA	OFILK	NA	1	NA	0.889 ± 0.045	32.18 ± 2.91	0.033 ± 0.018	0.886 ± 0.046	32.16 ± 2.91	0.033 ± 0.018	0.879 ± 0.049	32.03 ± 2.88	0.034 ± 0.018
vSHARP	It-equi	NA	OFTVLI	NA	1	NA	0.891 ± 0.042	30.62 ± 3.09	0.049 ± 0.030	0.888 ± 0.044	30.51 ± 3.08	0.051 ± 0.031	0.881 ± 0.046	30.33 ± 3.04	0.053 ± 0.032
vSHARP	It-equi	NA	DEMONS	NA	1	NA	0.891 ± 0.045	30.77 ± 2.89	0.045 ± 0.023	0.889 ± 0.046	30.81 ± 2.90	0.045 ± 0.023	0.884 ± 0.048	30.84 ± 2.87	0.045 ± 0.023

Table 1: Quantitative results for various configurations on the cardiac cine test set (under phase-specific settings).

Model	Reconstruction		Sampling		Registration		Joint		Loss		Weights		4x		6x		8x	
	Type	Initialization	Module	Loss	α	β	SSIM (↑)	PSNR (↑)	NMSE (↓)	SSIM (↑)	PSNR (↑)	NMSE (↓)	SSIM (↑)	PSNR (↑)	NMSE (↓)	SSIM (↑)	PSNR (↑)	NMSE (↓)
vSHARP	Adaptive	✗	Learned	✓	1	1	0.877 ± 0.050	31.68 ± 2.86	0.037 ± 0.019	0.867 ± 0.019	0.867 ± 0.019	0.854 ± 0.054	31.01 ± 2.69	0.042 ± 0.020				
vSHARP	Adaptive	✗	Learned	✗	1	1	0.880 ± 0.048	31.95 ± 2.81	0.034 ± 0.018	0.872 ± 0.049	31.75 ± 2.70	0.035 ± 0.017	0.862 ± 0.052	31.41 ± 2.64	0.038 ± 0.018			
vSHARP	Adaptive	✓	Learned	✓	1	1	0.882 ± 0.049	31.90 ± 2.92	0.035 ± 0.019	0.874 ± 0.051	31.75 ± 2.84	0.036 ± 0.019	0.862 ± 0.054	31.40 ± 2.75	0.039 ± 0.020			
vSHARP	Adaptive	✓	Learned	✗	1	1	0.881 ± 0.049	31.92 ± 2.91	0.035 ± 0.019	0.873 ± 0.051	31.73 ± 2.79	0.036 ± 0.018	0.861 ± 0.054	31.35 ± 2.75	0.039 ± 0.020			
vSHARP	Equi	NA	Learned	✓	1	1	0.879 ± 0.050	31.62 ± 2.98	0.038 ± 0.021	0.868 ± 0.053	31.51 ± 2.88	0.038 ± 0.020	0.848 ± 0.057	30.93 ± 2.72	0.043 ± 0.021			
vSHARP	Equi	NA	Learned	✗	1	1	0.881 ± 0.050	31.75 ± 3.00	0.037 ± 0.020	0.869 ± 0.054	31.62 ± 2.91	0.037 ± 0.020	0.849 ± 0.057	31.05 ± 2.74	0.042 ± 0.020			
vSHARP	Optimized	✗	Learned	✓	1	1	0.886 ± 0.047	32.17 ± 2.87	0.033 ± 0.018	0.879 ± 0.048	31.96 ± 2.80	0.034 ± 0.018	0.870 ± 0.050	31.71 ± 2.72	0.036 ± 0.018			
VarNet	Adaptive	✗	Learned	✓	1	1	0.837 ± 0.056	30.92 ± 2.40	0.041 ± 0.015	0.832 ± 0.057	30.77 ± 2.40	0.043 ± 0.016	0.829 ± 0.058	30.66 ± 2.38	0.044 ± 0.016			
vSHARP	Adaptive	✗	OFILK	NA	1	NA	0.868 ± 0.049	31.53 ± 2.68	0.037 ± 0.019	0.856 ± 0.052	31.15 ± 2.85	0.041 ± 0.019	0.842 ± 0.056	30.70 ± 2.62	0.045 ± 0.021			
vSHARP	Adaptive	✗	OFTVLI	NA	1	NA	0.873 ± 0.045	30.01 ± 2.78	0.055 ± 0.031	0.861 ± 0.049	29.55 ± 2.76	0.061 ± 0.034	0.848 ± 0.053	29.01 ± 2.77	0.069 ± 0.038			
vSHARP	Adaptive	✗	DEMONS	NA	1	NA	0.873 ± 0.050	30.36 ± 2.80	0.049 ± 0.024	0.863 ± 0.053	30.19 ± 2.78	0.051 ± 0.025	0.852 ± 0.056	29.93 ± 2.73	0.054 ± 0.026			
vSHARP	Equi	NA	OFILK	NA	1	NA	0.877 ± 0.046	31.82 ± 2.74	0.035 ± 0.018	0.861 ± 0.050	31.43 ± 2.65	0.038 ± 0.018	0.838 ± 0.055	30.72 ± 2.50	0.044 ± 0.019			
vSHARP	Equi	NA	OFTVLI	NA	1	NA	0.882 ± 0.044	30.40 ± 2.99	0.051 ± 0.031	0.868 ± 0.047	30.06 ± 2.87	0.054 ± 0.031	0.847 ± 0.052	29.32 ± 2.72	0.064 ± 0.035			
vSHARP	Equi	NA	DEMONS	NA	1	NA	0.880 ± 0.048	30.55 ± 2.83	0.047 ± 0.024	0.865 ± 0.052	30.32 ± 2.77	0.050 ± 0.024	0.845 ± 0.056	29.89 ± 2.64	0.054 ± 0.025			

Table 2: Quantitative results for various configurations on the cardiac cine test set (under unified sampling settings).

Model	Reconstruction		Sampling		Registration		Joint		Loss				Weights			
	Type	Initialization	Module	Loss	α	β	SSIM (\uparrow)	PSNR (\uparrow)	NMSE (\downarrow)	SSIM (\uparrow)	PSNR (\uparrow)	NMSE (\downarrow)	SSIM (\uparrow)	PSNR (\uparrow)	NMSE (\downarrow)	
vSHARP	Adaptive	\times	Learned	\checkmark	1	1	0.859 \pm 0.082	31.96 \pm 3.65	0.059 \pm 0.042	0.859 \pm 0.082	32.04 \pm 3.67	0.058 \pm 0.041	0.857 \pm 0.082	32.07 \pm 3.68	0.058 \pm 0.041	
vSHARP	Adaptive	\times	Learned (L)	\checkmark	1	1	0.860 \pm 0.081	31.93 \pm 3.57	0.059 \pm 0.040	0.860 \pm 0.080	32.03 \pm 3.58	0.058 \pm 0.039	0.858 \pm 0.079	32.03 \pm 3.57	0.057 \pm 0.039	
vSHARP	Adaptive	\times	Voxelmorph	\checkmark	1	1	0.839 \pm 0.085	31.10 \pm 3.40	0.069 \pm 0.044	0.835 \pm 0.086	31.05 \pm 3.42	0.070 \pm 0.044	0.830 \pm 0.086	30.94 \pm 3.42	0.071 \pm 0.044	
vSHARP	Adaptive	\times	Transfmorph	\checkmark	1	1	0.835 \pm 0.092	30.46 \pm 3.48	0.083 \pm 0.060	0.834 \pm 0.091	30.53 \pm 3.48	0.082 \pm 0.059	0.835 \pm 0.091	30.65 \pm 3.51	0.080 \pm 0.058	
vSHARP	Adaptive	\times	Learned	\checkmark	1	3	0.891 \pm 0.067	34.36 \pm 3.82	0.034 \pm 0.023	0.887 \pm 0.069	34.18 \pm 3.83	0.035 \pm 0.023	0.882 \pm 0.070	33.93 \pm 3.80	0.037 \pm 0.024	
vSHARP	Adaptive	\times	Learned	\times	1	1	0.860 \pm 0.080	32.00 \pm 3.58	0.058 \pm 0.041	0.859 \pm 0.080	32.05 \pm 3.59	0.058 \pm 0.040	0.857 \pm 0.080	32.04 \pm 3.59	0.058 \pm 0.039	
vSHARP	Adaptive	\checkmark	Learned	\checkmark	1	1	0.858 \pm 0.083	31.87 \pm 3.61	0.060 \pm 0.041	0.858 \pm 0.082	31.95 \pm 3.62	0.059 \pm 0.040	0.855 \pm 0.082	31.90 \pm 3.58	0.059 \pm 0.040	
vSHARP	Adaptive	\checkmark	Learned	\times	1	1	0.855 \pm 0.083	31.56 \pm 3.59	0.065 \pm 0.046	0.855 \pm 0.082	31.65 \pm 3.59	0.064 \pm 0.045	0.852 \pm 0.082	31.64 \pm 3.56	0.063 \pm 0.044	
vSHARP	Equi	NA	Learned	\checkmark	1	1	0.849 \pm 0.086	31.13 \pm 3.53	0.071 \pm 0.049	0.851 \pm 0.086	31.25 \pm 3.53	0.069 \pm 0.048	0.847 \pm 0.087	31.24 \pm 3.52	0.069 \pm 0.047	
vSHARP	Equi	NA	Learned	\times	1	1	0.849 \pm 0.087	31.12 \pm 3.55	0.072 \pm 0.050	0.849 \pm 0.087	31.18 \pm 3.52	0.070 \pm 0.049	0.844 \pm 0.087	31.15 \pm 3.49	0.070 \pm 0.048	
vSHARP	<i>k</i> -t-Equi	NA	Learned	\checkmark	1	1	0.847 \pm 0.086	31.19 \pm 3.56	0.070 \pm 0.049	0.847 \pm 0.085	31.27 \pm 3.53	0.069 \pm 0.047	0.839 \pm 0.087	31.20 \pm 3.55	0.069 \pm 0.047	
vSHARP	<i>k</i> -t-Equi	NA	Learned	\times	1	1	0.847 \pm 0.087	31.03 \pm 3.54	0.073 \pm 0.050	0.848 \pm 0.086	31.11 \pm 3.50	0.071 \pm 0.048	0.841 \pm 0.089	31.06 \pm 3.51	0.071 \pm 0.048	
vSHARP	Optimized	\times	Learned	\checkmark	1	1	0.863 \pm 0.081	32.20 \pm 3.60	0.055 \pm 0.037	0.863 \pm 0.080	32.26 \pm 3.58	0.054 \pm 0.036	0.861 \pm 0.080	32.25 \pm 3.56	0.054 \pm 0.035	
VarNet	Adaptive	\times	Learned	\checkmark	1	1	0.835 \pm 0.083	31.42 \pm 3.25	0.060 \pm 0.031	0.811 \pm 0.087	30.57 \pm 3.07	0.071 \pm 0.031	0.807 \pm 0.089	30.34 \pm 2.99	0.074 \pm 0.031	
vSHARP	Adaptive	\times	OFILK	NA	1	NA	0.829 \pm 0.089	30.41 \pm 3.25	0.081 \pm 0.053	0.827 \pm 0.089	30.42 \pm 3.23	0.081 \pm 0.052	0.825 \pm 0.089	30.41 \pm 3.20	0.081 \pm 0.051	
vSHARP	Adaptive	\times	OFTVLI	NA	1	NA	0.817 \pm 0.071	28.11 \pm 2.32	0.129 \pm 0.064	0.814 \pm 0.071	28.02 \pm 2.28	0.132 \pm 0.065	0.811 \pm 0.070	27.93 \pm 2.27	0.134 \pm 0.065	
vSHARP	Adaptive	\times	DEMONS	NA	1	NA	0.848 \pm 0.087	30.58 \pm 3.74	0.085 \pm 0.072	0.847 \pm 0.087	30.57 \pm 3.72	0.085 \pm 0.070	0.844 \pm 0.087	30.55 \pm 3.71	0.085 \pm 0.069	
vSHARP	Equi	NA	OFILK	NA	1	NA	0.827 \pm 0.091	30.37 \pm 3.29	0.082 \pm 0.054	0.826 \pm 0.091	30.40 \pm 3.26	0.081 \pm 0.052	0.821 \pm 0.092	30.33 \pm 3.21	0.082 \pm 0.050	
vSHARP	Equi	NA	OFTVLI	NA	1	NA	0.819 \pm 0.072	28.12 \pm 2.32	0.128 \pm 0.063	0.817 \pm 0.072	28.05 \pm 2.29	0.130 \pm 0.063	0.808 \pm 0.074	27.81 \pm 2.27	0.136 \pm 0.064	
vSHARP	Equi	NA	DEMONS	NA	1	NA	0.848 \pm 0.088	30.54 \pm 3.76	0.086 \pm 0.074	0.847 \pm 0.089	30.55 \pm 3.72	0.085 \pm 0.071	0.841 \pm 0.090	30.49 \pm 3.65	0.085 \pm 0.067	
vSHARP	<i>k</i> -t-Equi	NA	OFILK	NA	1	NA	0.826 \pm 0.091	30.36 \pm 3.30	0.082 \pm 0.054	0.824 \pm 0.091	30.37 \pm 3.28	0.082 \pm 0.053	0.816 \pm 0.063	30.30 \pm 3.24	0.082 \pm 0.051	
vSHARP	<i>k</i> -t-Equi	NA	OFTVLI	NA	1	NA	0.815 \pm 0.073	28.11 \pm 2.35	0.129 \pm 0.064	0.810 \pm 0.073	27.98 \pm 2.33	0.133 \pm 0.065	0.798 \pm 0.076	27.67 \pm 2.32	0.142 \pm 0.067	
vSHARP	<i>k</i> -t-Equi	NA	DEMONS	NA	1	NA	0.847 \pm 0.088	30.54 \pm 3.77	0.086 \pm 0.073	0.845 \pm 0.088	30.53 \pm 3.73	0.086 \pm 0.071	0.837 \pm 0.090	30.48 \pm 3.68	0.085 \pm 0.065	

Table 3: Quantitative results for various configurations on the aorta inference set (under phase-specific settings).

Model	Reconstruction		Sampling		Registration		Joint		Loss						
	Type	Initialization	Module	Loss	α	β	SSIM (↑)	NMSE (↓)	PSNR (↑)	SSIM (↓)	NMSE (↓)	PSNR (↑)			
	Weights														
vSHARP	Adaptive	✗	Learned	✓	1	1	0.837 ± 0.088	30.79 ± 3.45	0.075 ± 0.051	0.825 ± 0.090	30.49 ± 3.33	0.079 ± 0.049	0.809 ± 0.092	30.04 ± 3.23	0.085 ± 0.049
vSHARP	Adaptive	✗	Learned	✗	1	1	0.837 ± 0.086	30.85 ± 3.38	0.074 ± 0.049	0.827 ± 0.086	30.56 ± 3.29	0.077 ± 0.047	0.813 ± 0.088	30.18 ± 3.17	0.082 ± 0.046
vSHARP	Adaptive	✓	Learned	✓	1	1	0.841 ± 0.087	30.91 ± 3.49	0.074 ± 0.052	0.832 ± 0.086	30.77 ± 3.41	0.075 ± 0.050	0.820 ± 0.087	30.43 ± 3.30	0.079 ± 0.049
vSHARP	Adaptive	✓	Learned	✗	1	1	0.840 ± 0.087	30.88 ± 3.43	0.074 ± 0.049	0.830 ± 0.087	30.67 ± 3.32	0.076 ± 0.048	0.816 ± 0.089	30.29 ± 3.23	0.080 ± 0.047
vSHARP	Equi	NA	Learned	✓	1	1	0.837 ± 0.090	30.67 ± 3.50	0.078 ± 0.054	0.828 ± 0.091	30.59 ± 3.40	0.079 ± 0.052	0.803 ± 0.093	29.90 ± 3.14	0.088 ± 0.051
vSHARP	Equi	NA	Learned	✗	1	1	0.840 ± 0.090	30.83 ± 3.55	0.076 ± 0.054	0.831 ± 0.091	30.73 ± 3.46	0.076 ± 0.052	0.805 ± 0.094	30.07 ± 3.24	0.085 ± 0.051
VarNet	Adaptive	✗	Learned	✓	1	1	0.782 ± 0.089	29.56 ± 2.80	0.086 ± 0.028	0.769 ± 0.090	29.15 ± 2.69	0.094 ± 0.029	0.763 ± 0.089	28.97 ± 2.66	0.098 ± 0.030
vSHARP	Adaptive	✗	OFILK	NA	1	NA	0.810 ± 0.092	29.95 ± 3.09	0.087 ± 0.052	0.795 ± 0.092	29.53 ± 2.93	0.094 ± 0.050	0.776 ± 0.092	29.04 ± 2.80	0.102 ± 0.048
vSHARP	Adaptive	✗	OFTVLI	NA	1	NA	0.792 ± 0.072	27.52 ± 2.20	0.145 ± 0.065	0.771 ± 0.072	26.97 ± 2.12	0.162 ± 0.069	0.747 ± 0.071	26.44 ± 2.07	0.181 ± 0.073
vSHARP	Adaptive	✗	DEMONS	NA	1	NA	0.832 ± 0.090	30.13 ± 3.57	0.091 ± 0.071	0.817 ± 0.091	29.72 ± 3.39	0.096 ± 0.069	0.800 ± 0.093	29.28 ± 3.23	0.103 ± 0.066
vSHARP	Equi	NA	OFILK	NA	1	NA	0.820 ± 0.091	30.22 ± 3.27	0.084 ± 0.054	0.806 ± 0.092	29.98 ± 3.14	0.088 ± 0.053	0.778 ± 0.093	29.38 ± 2.92	0.097 ± 0.050
vSHARP	Equi	NA	OFTVLI	NA	1	NA	0.809 ± 0.073	28.00 ± 2.33	0.132 ± 0.064	0.792 ± 0.074	27.64 ± 2.27	0.141 ± 0.066	0.758 ± 0.074	26.87 ± 2.17	0.165 ± 0.068
vSHARP	Equi	NA	DEMONS	NA	1	NA	0.840 ± 0.090	30.40 ± 3.73	0.088 ± 0.074	0.826 ± 0.092	30.14 ± 3.62	0.091 ± 0.072	0.797 ± 0.094	29.50 ± 3.34	0.100 ± 0.067
vSHARP	Optimized	✗	Learned	✓	1	1	0.846 ± 0.085	31.15 ± 3.51	0.070 ± 0.049	0.838 ± 0.086	30.85 ± 3.41	0.073 ± 0.048	0.828 ± 0.086	30.59 ± 3.31	0.076 ± 0.047

Table 4: Quantitative results for various configurations on the aorta inference set (under unified sampling settings).

C.2 Additional Figures

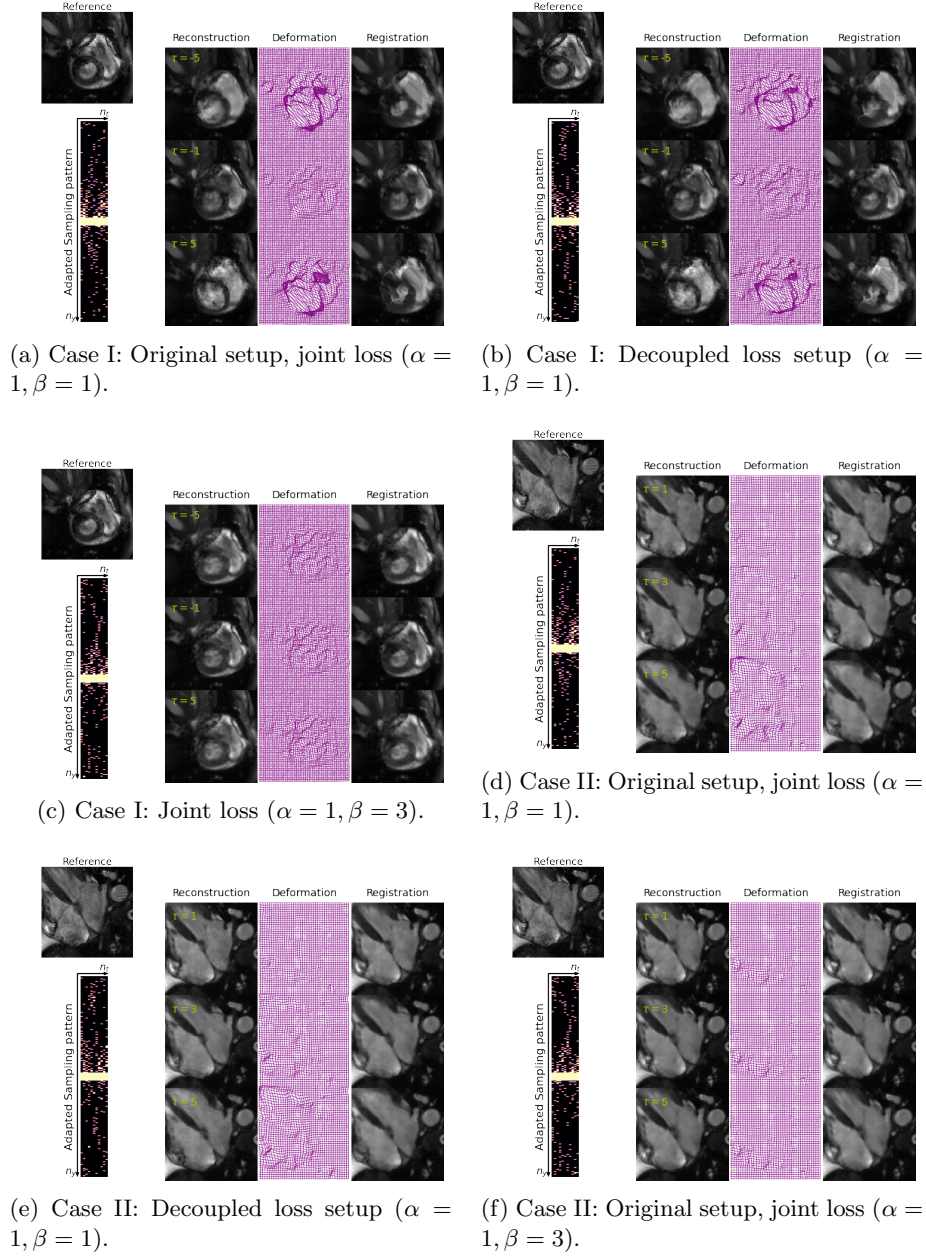


Fig. 13: Example results for two cases, shown at various temporal frames (τ) relative to the reference image, for different loss function setups at $R = 8$.

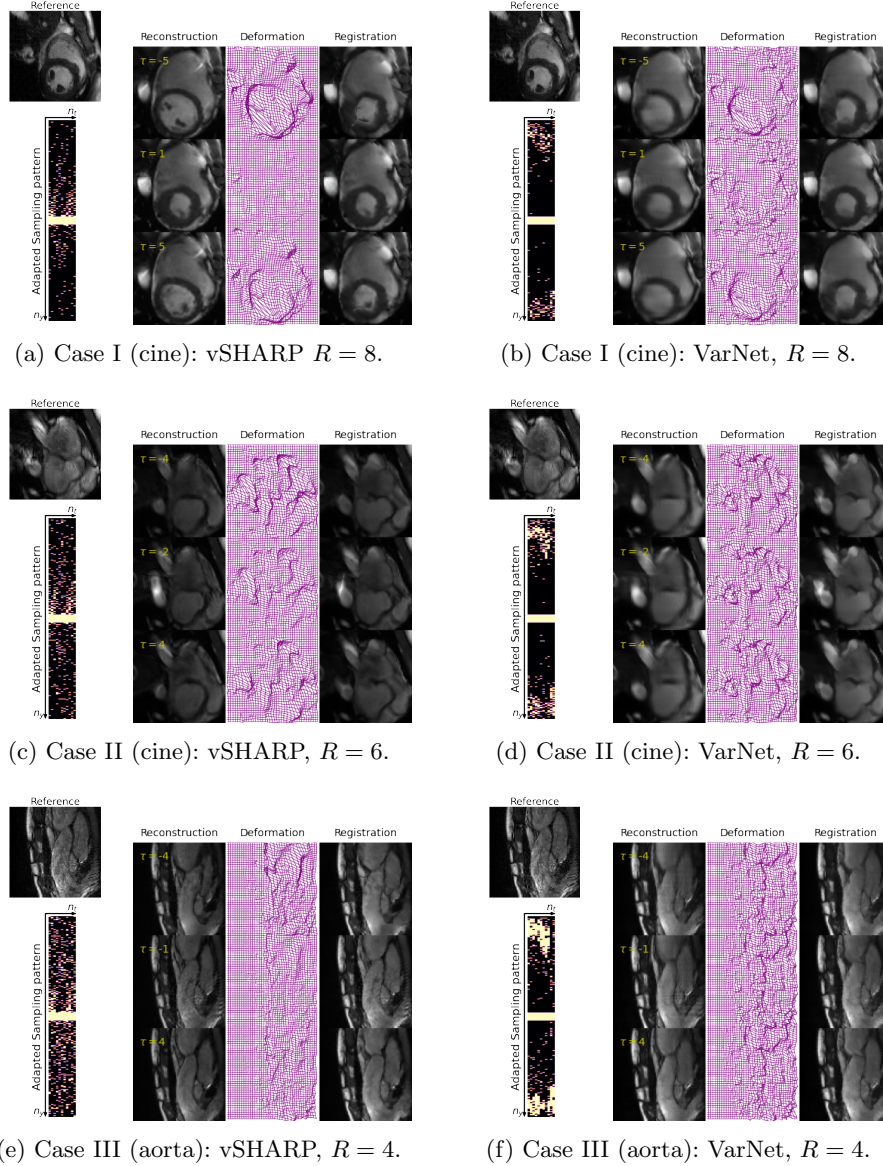


Fig. 14: Example results for three cases, for shown at various temporal frames (τ) relative to the reference image, for different choices of reconstruction network at different accelerations.

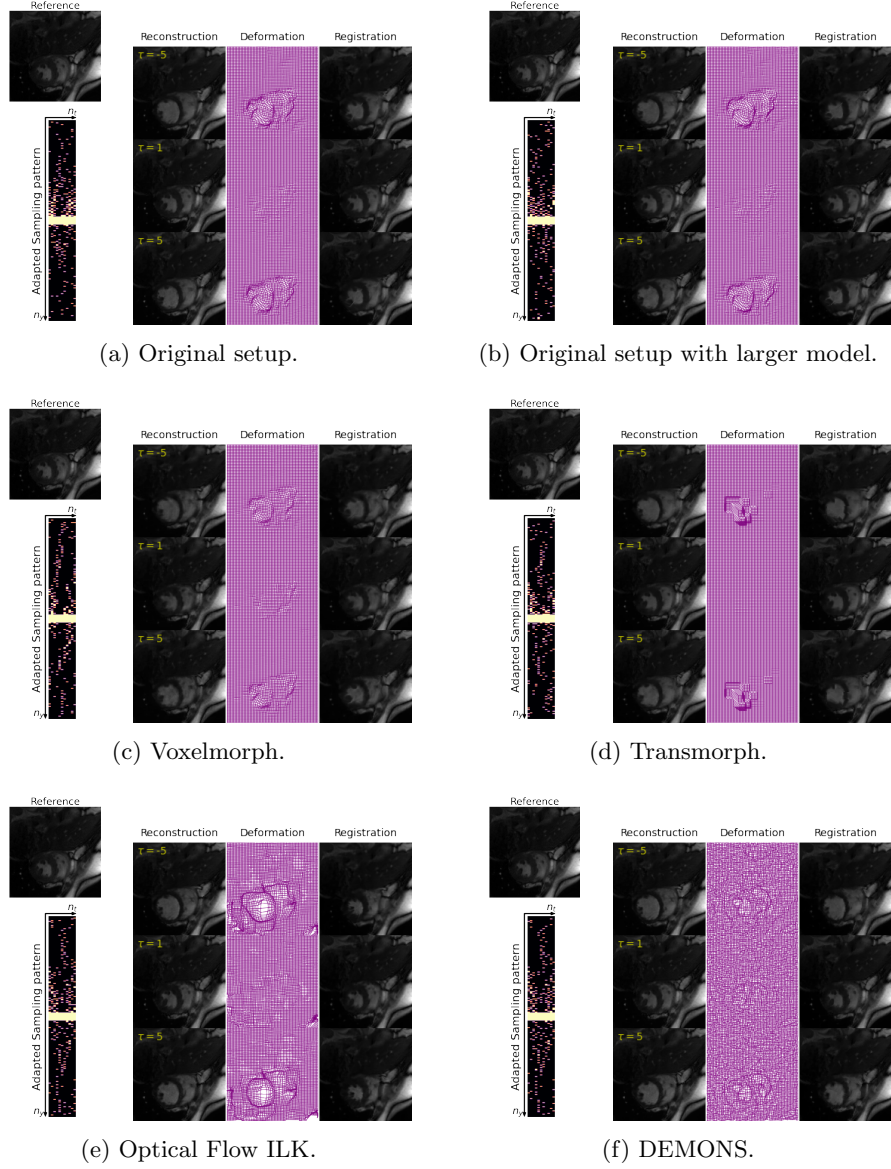


Fig. 15: Example results I for a cardiac cine case, shown at various temporal frames (τ) relative to the reference image, for different choices of registration network at $R = 8$.

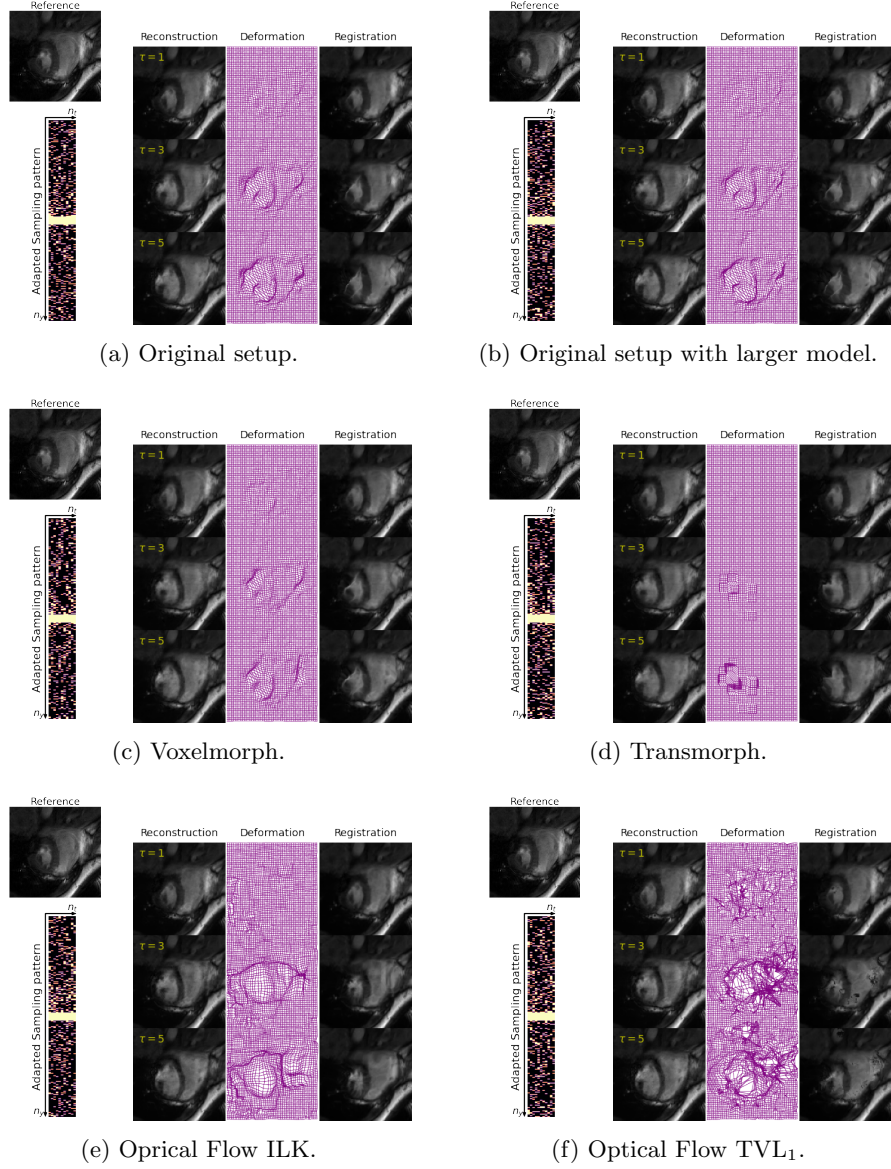
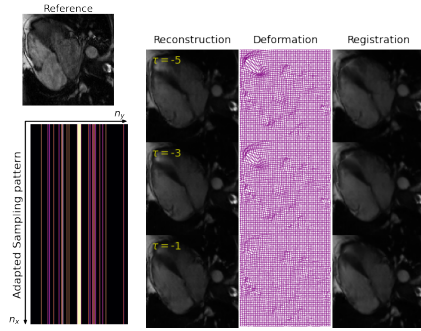


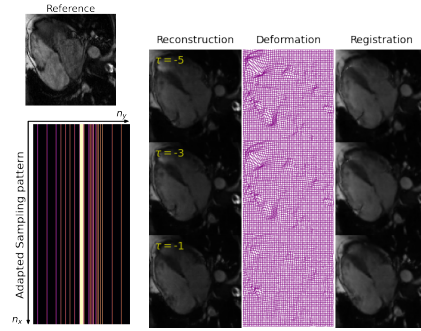
Fig. 16: Example results II for a cardiac cine case, shown at various temporal frames (τ) relative to the reference image, for different choices of registration network at $R = 4$.



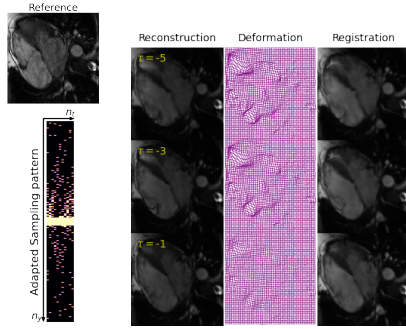
Fig. 17: Example results III for an aorta case, shown at various temporal frames (τ) relative to the reference image, for different choices of registration network at $R = 6$.



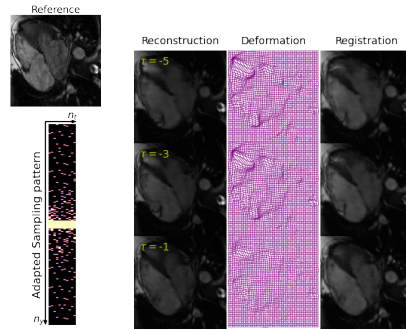
(a) Unified sampling.



(b) Unified sampling with initialization.



(c) Phase-specific sampling.



(d) Phase-specific sampling with initialization.

Fig. 18: Example results I for a cardiac cine case, shown at various temporal frames (τ) relative to the reference image, for different choices of adaptive sampling at $R = 8$.

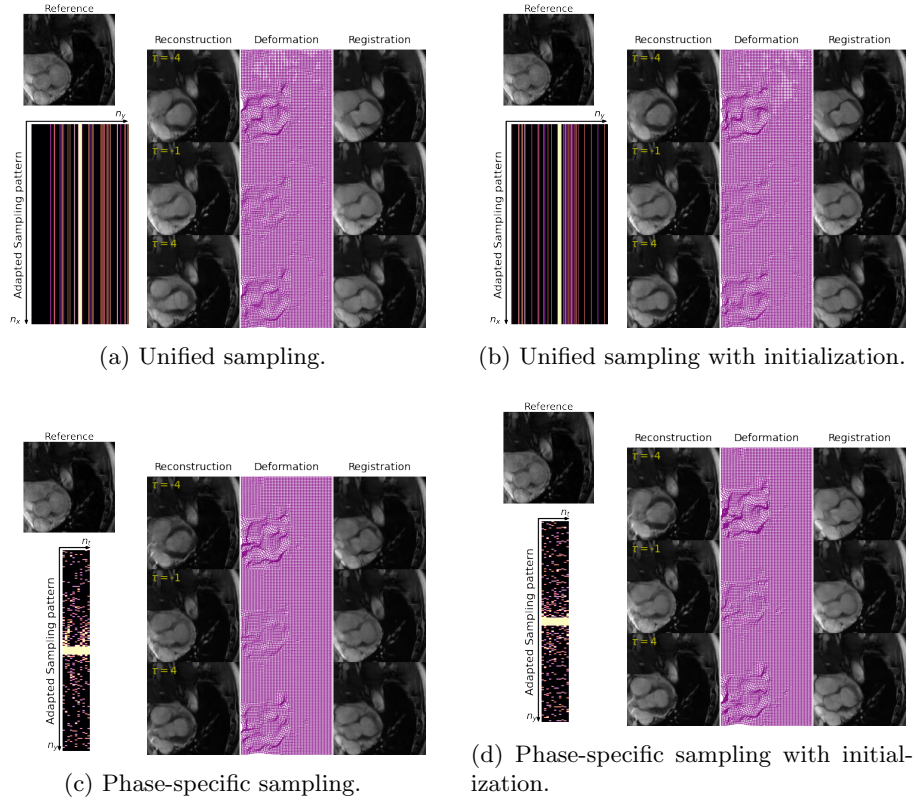


Fig. 19: Example results II for a cardiac cine case, shown at various temporal frames (τ) relative to the reference image, for different choices of adaptive sampling at $R = 6$.